Mechanical Design, Dynamic Modeling and Control of Hydraulic Artificial Muscles

by

Arman Nikkhah
Bachelor of Science, University of Tehran, 2016

A Thesis Submitted in Partial Fulfilment of the Requirements
for the Degree of
MASTER OF APPLIED SCIENCE
in the Department of Mechanical Engineering

Supervisory Committee

Mechanical Design, Dynamic Modeling and Control of
Hydraulic Artificial Muscles

by
Arman Nikkhah
Bachelor of Science, University of Tehran, 2016

Supervisory Committee

Dr. Colin Bradley, Department of Mechanical Engineering

Supervisor

Dr. Daniela Constantinescu, Department of Mechanical Engineering

Departmental Member

Abstract

Artificial human muscles have traditionally been operated through pneumatic means, and are known as Pneumatic Artificial Muscles (PAMs). Over the last several decades, Hydraulic Artificial Muscles (HAMs) have also been investigated due to their high power-to-weight ratio and human-like characteristics. Compared to PAMs, HAMs typically exhibit faster response, higher efficiency, and superior position control; characteristics which provide potential for application in rehabilitation robotics. This thesis presents a new approach to actuate artificial muscles in an antagonistic pair configuration. The detailed mechanical design of the test platform is introduced, along with the development of a dynamic model for actuating an artificial elbow joint. Also, custom manufactured Oil-based Hydraulic Artificial Muscles (OHAMs) are implemented in a biceps-triceps configuration and characterized on the test platform. Furthermore, an integrator-backstepping controller is derived for HAMs with different characteristics (stiffness and damping coefficients) in an antagonistic pair configuration. Finally, simulations and experimental results of the position control of the artificial elbow joint are discussed to confirm the functionality of the OHAMs utilizing the proposed actuating mechanism and the effectiveness of the developed control algorithm.

Contents

List of Figures

List of Tables

Acknowledgements

I would like to express my deepest appreciation to Prof. Colin Bradley for his patience, motivation, enthusiasm and immense knowledge. His guidance helped me all the time of my research at the University of Victoria. I could not have imagined a better advisor for my M.A.Sc. graduate studies.

This thesis is dedicated to my beloved parents

without whom none of my successes would have been possible.

Chapter 1

Introduction

In this chapter, a brief history of artificial muscles is presented in the background section which includes description, application and types of artificial muscles. Moreover, the main objectives of the thesis are discussed in the second section of this chapter.

1.1 Background

Joseph L. Mckibben invented the Pneumatic Artificial Muscle (PAM) in 1961 and this invention provided researchers with new opportunities for investigating human-like actuators [70, 50]. The Japanese tire manufacturer Bridgestone introduced a more powerful version of the PAM, called Rubbertuator, in 1988 [29]. The schematic of this manipulator utilizing PAMs is shown in Figure 1.1.

1.1.1 Description of artificial muscles

An artificial muscle actuator is a mechanical device that mimics the behaviour of skeletal muscle in that it contracts and generates force in a non-linear manner when activated. Artificial muscles are constructed of a tubular shaped rubber bladder and an inextensible fiber mesh that either surrounds or is embedded in the rubber matrix. The fiber mesh provides support and enhances actuation. The rubber bladder is completely sealed except for a valve that allows fluids to enter and exit. Once pressurized, the artificial muscle expands in a

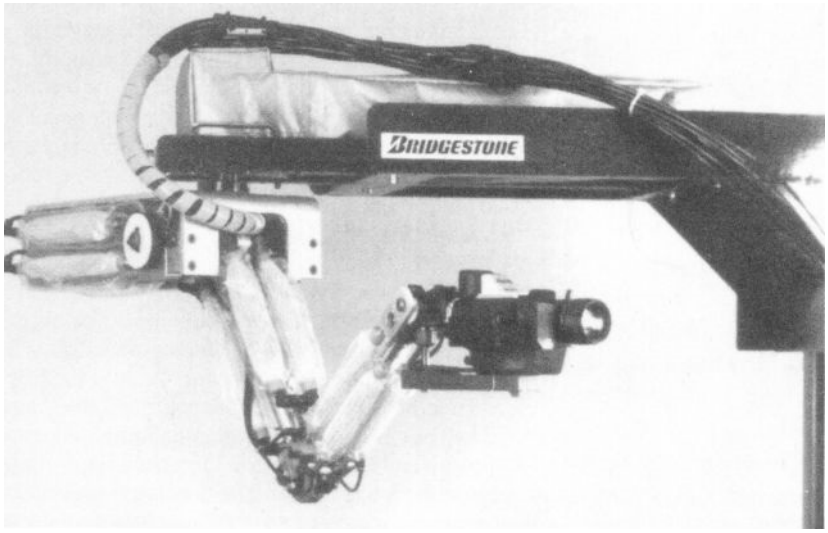

Figure 1.1: Rubbertuator by the Japanese tire manufacturer Bridgestone [29].

radial direction resulting in contraction and force production in the longitudinal direction. Figure 1.2 illustrates the operation of an artificial muscle in biceps-triceps configuration. The level of contraction and force production depend on the external mass which is attached to artificial muscle.

The artificial muscles have several characteristics that make them an ideal actuator for applications involving human-interaction. Artificial muscles are capable of generating high force outputs along with high power-to-weight and power-to-volume ratios than electric motors or hydraulic actuators [61]. Also, they have a higher output force rather than a pneumatic/hydraulic cylinder of equal volume. Artificial muscles are cost effective, clean, compact, and can be used in harsh environments because they do not have moving parts such as pistons or guiding rods. Artificial muscles can be used in microgravity environments, because gravity is not necessary to produce contraction or force generation. They are also a safe alternative to other actuators. They provide ”soft actuation” meaning safety is enhanced through a low mass structure that combines high strength with actuator [8]. Their ”soft actuation” allows them to be used in contact with humans without posing safety risks associated with other actuators that are mostly heavy and solid. The most challenging

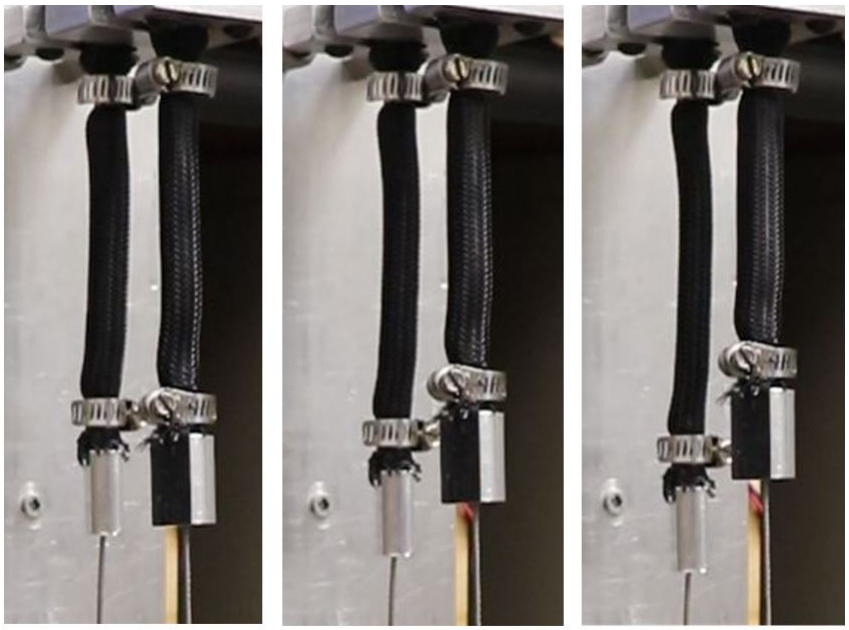

Figure 1.2: The operation of artificial muscles in biceps-triceps configuration. (a) Equal pressure in biceps and triceps artificial muscles. (b) Medium pressure in biceps artificial muscle. (c) Maximum pressure in biceps artificial muscle.

part in using artificial muscles is the difficulty involved with controlling them due to their non-linear dynamics and time varying behaviour. The main source of non-linearity can be explained by the basic operation of an artificial muscle. As pressure increases linearly, the tubing expands radially resulting in a non-linear increase in the tube's diameter. Thus the force will increase non-linearly [61].

1.1.2 Application of artificial muscles

Due to the PAMs dynamic properties and characteristics that mimic human muscle, there has been a renewed interest in PAM research, particularly applied to exoskeleton robots for rehabilitation and power augmentation. The Mckibben muscle consists of an inflatable membrane, enclosed within a helical-mesh sleeve, and secured with fittings at both ends [18]. The sleeve envelopes the membrane and provides a secure fit. PAMs operate at an overpressure and, as the inner elastic tube is pressurized, they radially expand exerting a

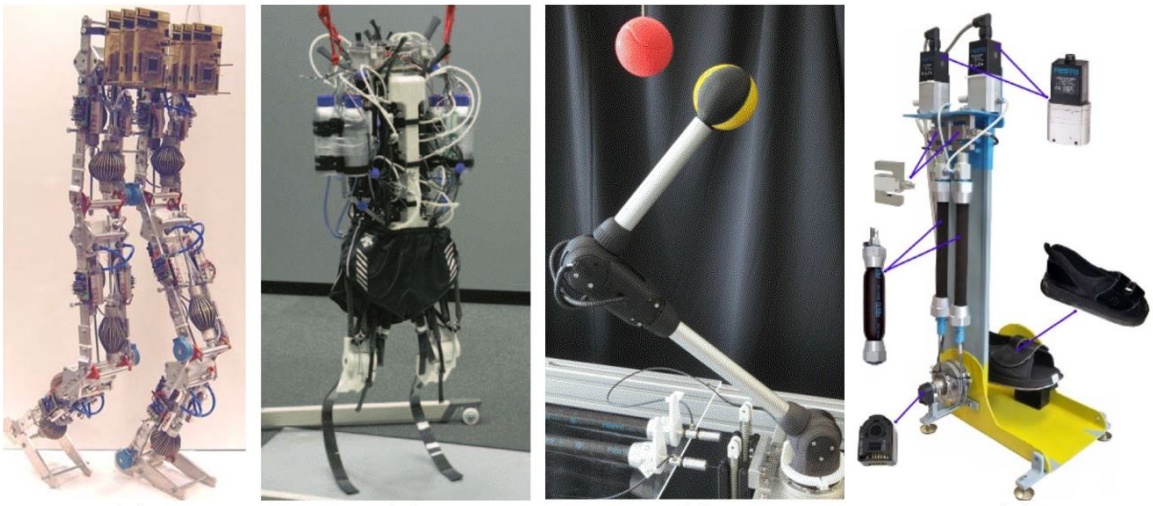

Figure 1.3: Different applications of PAMs. (a) Humanoid robots [83]. (b) Biped robots [51]. (c) Manipulators [6]. (d) Artificial limbs [46].

force on the sleeve. The tension within the sleeve accumulates at the PAM's fittings and a force is transferred to an external load through the intervening connectors and mechanism. PAMs have many advantages over conventional pneumatic cylinders such as high power-to-weight ratio, human-like characteristics, a self-limiting feature, and are comprised of inexpensive materials [25]. In the research literature, numerous applications of PAMs are described including artificial limbs [68, 36, 46], humanoid robots [31, 3], biped robots [83, 51, 52], and robotic arms [32, 6], so that their actuators have typically more power-to-weight ratio in comparison to traditional humanoid robots [56] or quadruped robots [55]. They are either single-muscle configuration [48, 59] or pair-muscle [22, 47] configuration. Different applications of PAMs are shown in Figure 1.3.

Hydraulic Artificial Muscles (HAMs) are a more recent development that employ an internally pressurized liquid. Several research groups have extended the capability of artificial muscles by utilizing water as the liquid within the membrane, thereby avoiding the use of bulky compressors [76]. Liquids offer the primary advantage that different liquid specifications result in different operating characteristics for the HAMs, which is beneficial for their dynamic and control [91]. Other advantages are faster response time and

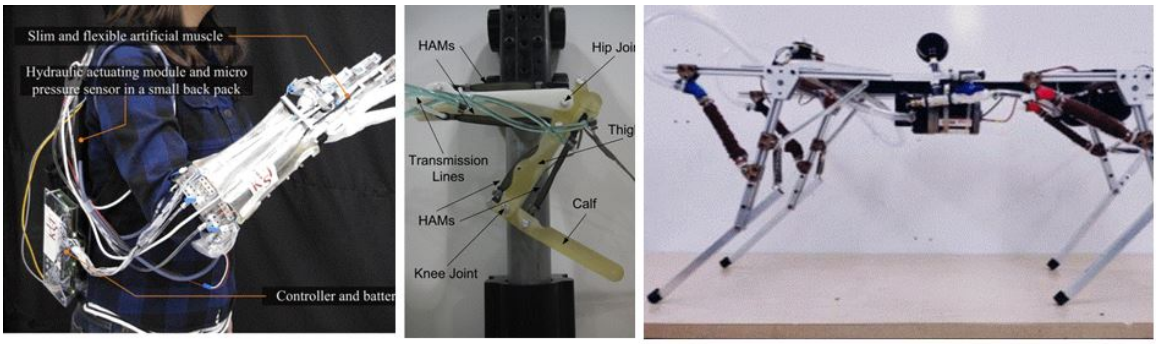

(a) (b) (c)

Figure 1.4: Different applications of HAMs. (a) Haptic gloves [65]. (b) Legged robots [76]. (c) Quadruped robots [74].

improved position control compared to PAMs due to hydraulic fluid's higher bulk modulus [21, 23]. Also, the lower compressibility of liquids (oil, water, etc.) than air is one of the reasons that inspired the use of a hydraulic fluid in order to increase the stiffness and efficiency of artificial muscles [21, 85, 39]. Microscale HAMs have been implemented in haptic gloves and are capable of generating forces with magnitudes of 5 N [65] and operate completely independently and the applicant can move freely while wearing it. HAMs have also been used in artificial limbs [45] in order to mimic the human-like range of motion and torque limitations. A water-based hydraulic artificial muscle (WHAM) with a high force-to-weight ratio and strength has recently been designed specifically for underwater vehicles [91]. A novel HAM was presented by Worcester Polytechnic Institute (WPI) researchers which has a greater efficiency compared to traditional PAMs. It has been implemented in different robotic systems like Elbow Exo-musculatures, Knee Exomusculature, a kangaroo robot, and a hydro dog robot [74].It is important to mention that the mechanical components of PAMs can also be used for HAMs in the same pressure range. Moreover, the dynamic modeling approaches for PAMs can be developed for HAMs, with some differences in stiffness and damping ratio, due to similar inherent characteristics in artificial muscles. Different applications of PAMs are shown in Figure 1.4. A comparison of previous research on HAMs, relative to this work, is shown in Table 1.1 with an emphasis on

muscle configuration, modeling approach and control method.

Table 1.1: Recent investigations on HAMs

Authors	Configuration	Modeling approach	Controller
This Platform	Bidirectional	Phenomenological	Integrator-Backstepping
Meller et al. [44]	Unidirectional	Energy Conservation	Cascaded PI-P with ff
Slightam et al. [73]	Unidirectional	Phenomenological	Sliding mode
Meller et al. [43]	Unidirectional	Energy Conservation	PI
Xiang et al. [85]	Unidirectional	Energy Conservation	PID
Kobayashi et al. [37]	Unidirectional	Phenomenological	MPC with RLS
Tiwari et al. [76]	Bidirectional	Energy Conservation	Open-loop
Focchi et al. [21]	Unidirectional	Phenomenological	Cascaded PI-P

1.1.3 Types of artificial muscles

Different studies have been developed on the typical rubber, fiber-mesh, and size of artificial muscles. These include McKibben muscles with braided fibers, straight fibers, and artificial muscles constructed of alternative elastomeric and fiber materials. Pleated artificial muscles have been developed where the pleating either runs along the length of the muscle or perpendicular to the length of the muscle. Also, Curved muscles have been studied where the rubber tube is no longer configured to be straight. Hybrid devices have incorporated springs with artificial muscles to act as a built-in antagonist, dampers and brakes designed to alter performance, and rings designed to increase contraction. Various artificial muscles are now commercially available.

McKibben muscle

Various groups have constructed artificial muscles with an inner rubber tube surrounded by a braided fiber mesh. The braided fibers are designed in a helical pattern and attached to the ends of the artificial muscle which is called McKibben muscle after Dr. Joseph McKibben popularized pneumatic muscle in 1950. Different tube lengths, diameters, fittings and ma-

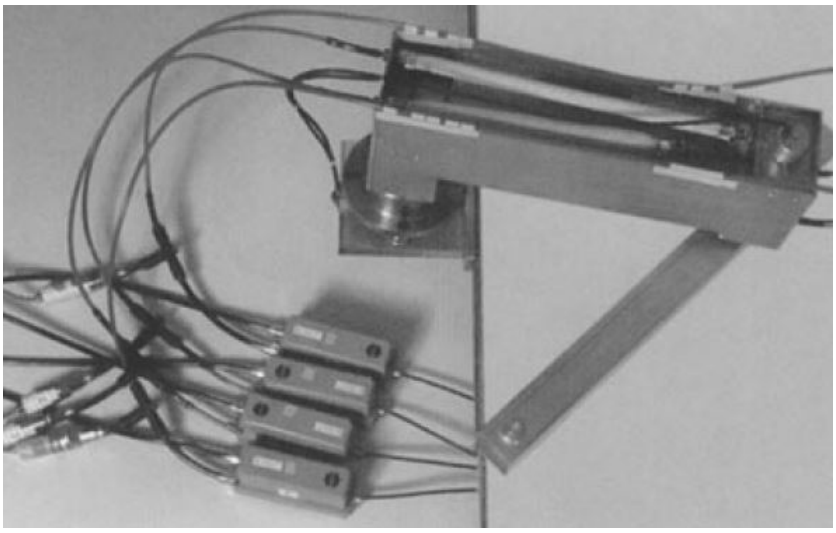

Figure 1.5: 2-DOF SCARA robot actuated by two pairs of McKibben muscles [77].

terials have been tested to construct McKibben muscles. In the following paragraph, some of well-known research projects utilizing McKibben muscles are presented.

One of the examples is a device with an inner layer made from thin-walled rubber tubing and an outer layer made from flexible sheathing formed from high-strength interwoven nylon fibers. Perspex plastic plugs are used as end fittings, sealing the two ends of the muscle. The nylon shell and rubber tubing are bonded to the end fittings utilizing a flexible adhesive and clamped securely in place using a rubber sealing ring [8]. Another example is a project in the University of Michigan in which artificial muscles are designed using latex tubing as the inner bladder, braided polyester sleeving as the muscle shell, plastic pneumatic fittings for the end fittings along with different valves [19]. The next example is a platform with artificial muscles with airtight inner tube surrounded by a braided mesh shell along with flexible inextensible threads (i.e. threads having very high longitudinal stiffness) attached at either end to fittings [13]. Also, a research group presented artificial muscles consist of an inner rubber tube surrounded by a double helix textile weave [77]. A 2-DOF robot actuated by two pairs of McKibben muscles is shown in Figure. 1.5.

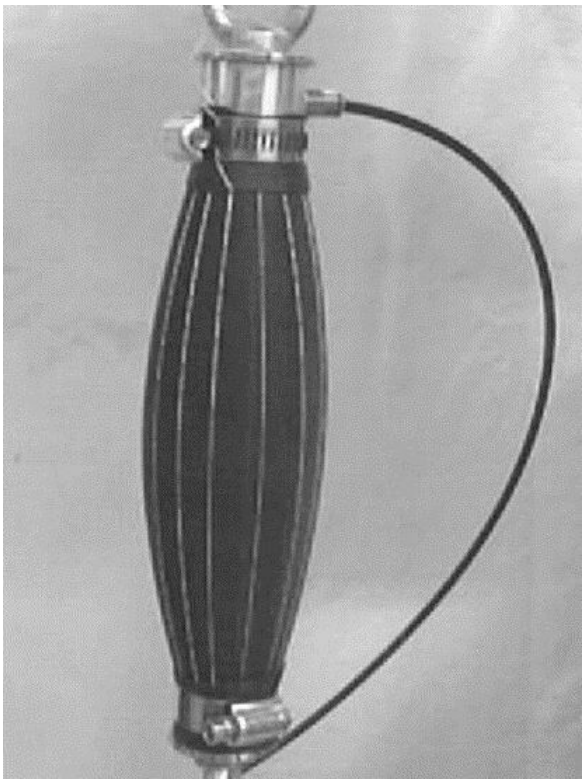

Figure 1.6: Schematic of an straight fiber artificial muscle [4].

Straight fiber artificial muscle

Straight fiber artificial muscle design has also been used in some research projects. Nakamura et al. have implemented pneumatic muscles reinforced by straight fibers. The designed devices have a central ring which is essential in the functionality of artificial muscles. Also, he reported that this type of muscle has a greater contraction ratio and a longer lifetime than conventional braided pneumatic muscles [49]. Bettetto et al. studied straight fiber artificial muscle utilizing Finite Element Method (FEM) and found out that straight fiber muscles can provide five times more tensile force than braided fiber muscles, but have a smaller contraction ratio [4]. An example of straight artificial muscle is shown in Figure. 1.6.

Pleated artificial muscle

A pleated artificial muscle has a unique structure in which there is no outer cover. The inner tube itself has pleats or folds. A pleated artificial muscle which has folds along the longitudinal axis of the muscle is investigated in the history of these artificial muscles. The folds hold the extra membrane material needed to expand. The membrane material has a high tensile stiffness in order to eliminate rubber-like strain. This type of pneumatic muscle has higher contraction forces and displacements than a braided artificial muscle actuator. Also, it has low friction, no friction-related hysteresis, and can operate at low pressures [26]. The fold faces are laid out radially so no friction is involved in the folding process, and no loss of force output occurs during the unfolding process because no appreciable amount of energy is needed to unfold. The pleated artificial muscle was used in the walking bipedal robot Lucy [83] as shown in Figure. 1.7. Another pleated pneumatic muscle was developed by Zhang et al., but here the pleats run perpendicular to the longitudinal axis of the muscle. This type of pleated artificial muscle actuator is referred to as a rubber bellows artificial muscle. The driving force of the actuator is determined by the size of the bellows and the internal pressure. The design of this actuator allows it to curve along its longitudinal axis easily, which is useful for joint design. The radial elastic expansion of the actuator is limited, but the longitudinal elastic expansion range is large due to fiber weaving inside the rubber bellows [89].

Curved artificial muscle

Curved artificial muscle is developed as a separate type of artificial muscle because of its unique configuration and model characterization. Zhang et al. have developed a curved pneumatic muscle actuator constructed from Festo brand fluidic muscle for use in a wearable elbow exoskeleton robot. The configuration of this artificial muscle is based on a rotary actuator. It weakens the coupling relationship between the output force and displacement

Figure 1.7: Schematic of deflated and inflated state of the Pleated Artificial Muscle [83].

so that feedback force can be achieved easily. New modeling techniques including beam modeling and membrane modeling had to be investigated to obtain a mathematical model of an artificial muscle in the curved configuration [90]. Trivedi et al. developed a soft robotic manipulator named OctArm V (Figure. 1.8) that can bend into a wide variety of complex shapes when reacting to control inputs. In this design, nine artificial muscles are used in a curved configuration. This researcher presented a new approach for modeling the dynamics of the curved artificial muscle manipulator that incorporates the effect of material non-linearities along with weight distribution [80].

Artificial muscles using alternative materials

Both alternative fiber materials and alternative elastomers have been used to construct artificial muscles. Alternative fiber materials include carbon [66], glass fiber [49], and shape memory alloy wires [84]. Wang et al. developed an intelligent artificial muscle utilizing shape memory alloy wires in the braided shell. The artificial muscle operates as a typical artificial muscle would until the shape memory alloy wires are activated (via a current

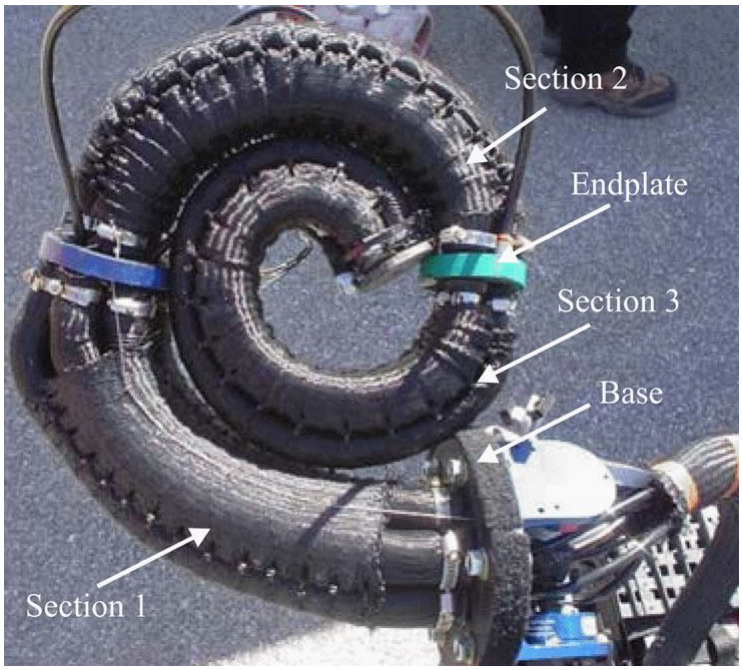

Figure 1.8: Schematic of OctArm V,a soft robotic manipulator, with artificial muscles in a curved configuration [80].

change). When activated, shape memory alloy wires contract, affecting movement of the braided shell and hence motion of the artificial muscle. Motion, contraction ratio, and force of the pneumatic muscle can therefore be adjusted by activating the shape memory alloy wires of the braided shell. Simulation results verify the intelligent artificial muscle has a higher contractile force per cross-sectional area and more flexible stiffness than a traditional pneumatic muscle. An artificial muscle developed by Goulbourne utilized a dielectric elastomer for the inner bladder of a pneumatic muscle. When activated by voltage, dielectric elastomer has a large strain actuation response ($> 100\%$), but a low force output. The low force output has limited its use for many applications, but by enclosing the dielectric elastomer in a helical network of inextensible fibers, the load-bearing capability of the dielectric elastomer improves. This electro-pneumatic actuator expands radially and contracts axially when activated by pressure and voltage [24]. An artificial muscle made of alternative material (carbon) is shown in Figure. 1.9.

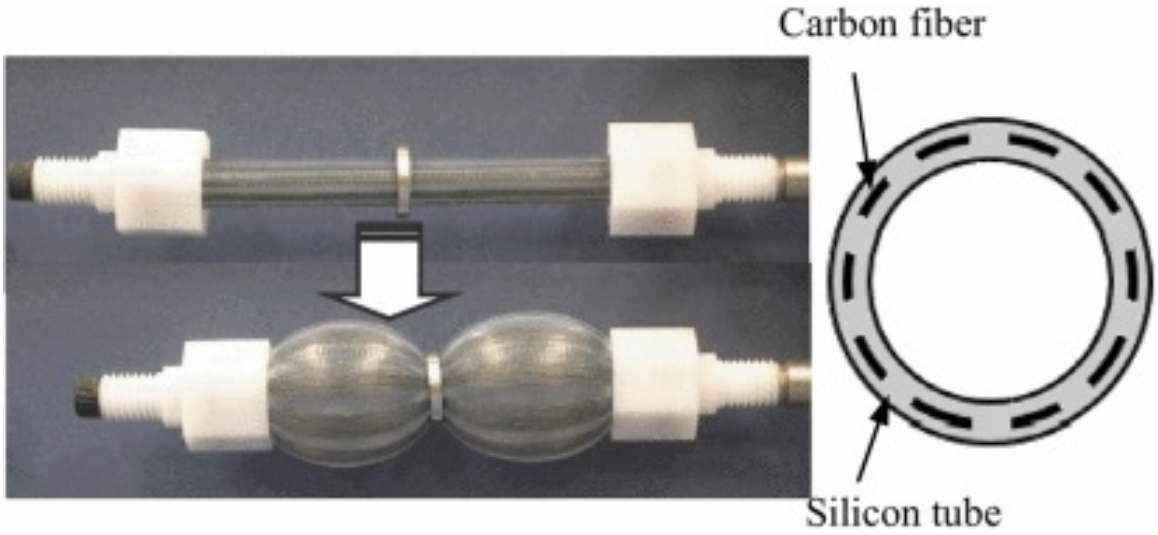

Figure 1.9: Schematic of an artificial muscle using alternative material (carbon) [66].

Commercially available artificial muscles

Commercially available artificial muscles include the fluidic muscle from Festo Corporation, the Air Muscle from Shadow Robot Company, and the Rubbertuator from Bridgestone. Many research groups have used Festo fluidic muscles in their platforms. Festo fluidic muscle is constructed of a three-dimensional rhomboidal woven fiber mesh embedded in a rubber bladder. This construction improves hysteresis, non-linearity and durability. Fluidic muscles are available in various diameters and a multitude of nominal lengths. The maximum contraction is approximately 25% of the nominal length. The largest artificial muscle is capable of lifting 6000 N (1349 lb) at its maximum pressure of 600 kpa (87.2 psi) [20]. The Air Muscle from Shadow Robot Company has an inner rubber tube encased in a plastic woven shell in various sizes. The largest model can generate forces up to 687 N (154 lb) at its maximum rated pressure of 400 kPa [71]. The Bridgestone Rubbertuator was first marketed in the 1980. Its structure was modeled after the McKibben muscle, but materials were chosen for improved robustness and performance. Bridgestone marketed two multi-joint robots that used Rubbertuators; a horizontal robot which is known as RASC and a suspended robot which is known as SoftArm. The practical use of these robots was

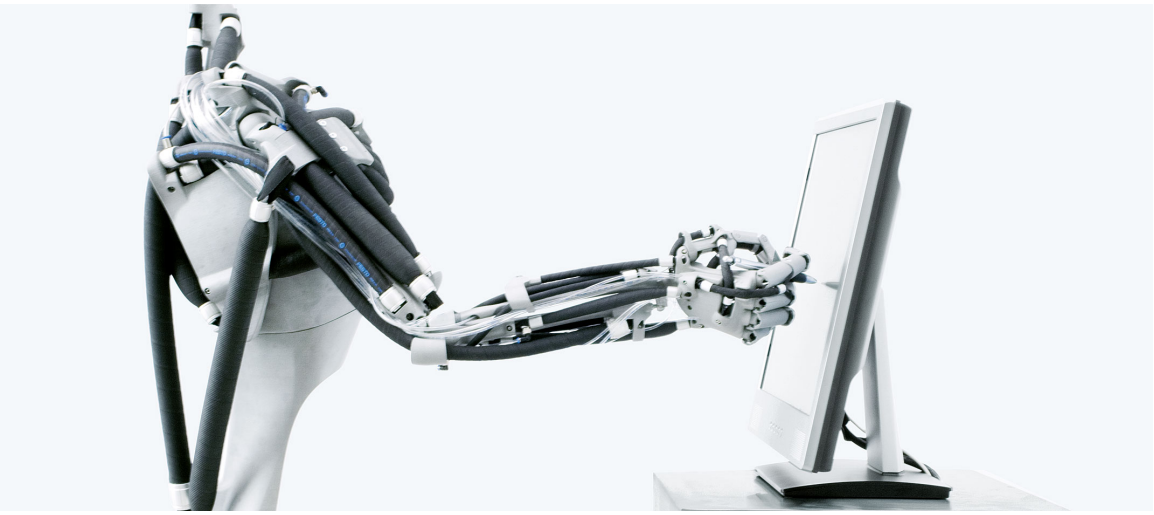

Figure 1.10: Schematic of Airic's arm, a bio-inspired robot, utilizing commercially available artificial muscles [20].

limited, and both arms were discontinued by the 1990s. Bridgestone Rubbertuator's are still being used today in physical rehabilitation robots [29]. Figure. 1.10 shows Airic's arm which is using commercially available artificial muscles.

1.2 Scope and contribution of this thesis

The first contribution of this work is a new mechanical design for actuating HAMs in an antagonistic pair configuration. In this design, common mechanical components in traditional designs (e.g. servo valve, relief valve, filters, pump, electro-motor, pressure transducer and tank) have been replaced by a linear actuator, two cylinders and two mechanical valves. As a result, the system can be disconnected from the source of fluid which provides the potential for a portable system. Moreover, the components of the platform operate at a pressure greater than the typical 700 kPa common in PAMs [21], which means that PAMs, or traditional McKibben muscles, are incompatible with liquid-based artificial muscles. In fact, liquid consumes less energy than air for operating the elbow joint since the mass flow is considerably less using oil. Also, the conventional limitations of water-based systems (e.g. corrosion, filtering, and low boiling point) have been removed due to implementation

of a robust mechanical test platform consisting of OHAMs, cylinders, fittings and support structures. The specification of all mechanical components of the actuating mechanism is presented in detail along with mechanical design of custom manufactured OHAMs in Chapter 2. The second contribution is providing a dynamic model for artificial muscles in an antagonistic pair (biceps-triceps) configuration for actuating an elbow joint. This modeling is based on phenomenological approach and can be implemented in different projects with various specifications which is presented in detail in Chapter 3. The third contribution of this research is introducing an integrator-backstepping controller for HAMs and PAMs in opposing-pair configuration which can be used for different systems with different stiffness values and damping ratios and it is presented in Chapter 4. In addition, the functionality of the presented actuating mechanism and artificial muscles are demonstrated by the implementation of OHAMs in an antagonistic pair configuration. Finally, the controller algorithm is implemented using parameter and functions extracted from system identification of the OHAM platform and characterizing the behaviour of the artificial muscles in an antagonistic pair configuration. The implementation of the system is discussed in detail in Chapter 5.

Chapter 2

Mechanical design

The OHAM platform is composed of horizontal and vertical members. The horizontal parts consist of one linear actuator, two linear cylinders, two pressure gages, and connectors. All components of the OHAM have been designed and assembled in the SolidWorks software, because it improves the way we develop and manufacture the OHAM platform. It covers design, simulation, cost estimation, manufacturability checks, and optimization of the final design. A motion simulation of the joints and links have been developed to find intersections of the components and the workspace of the elbow joint. Finally, the analyzed design has been selected for manufacturing. The mechanical design of the OHAM platform is shown in Figure 2.1. By pushing the linear actuator, the rocking arm, which is contacted to a motionless joint with similar distances to the effecting point of linear cylinders, is pushed as well. As a result, the nearest linear cylinder, which contains liquid (oil), will be pulled and it will pressurize its liquid which is connected to a OHAM. Consequently, the corresponding artificial muscle will be inflated due to specification of artificial muscles. At the same time, the other linear cylinder is pulled, and the corresponding artificial muscle is deflated on the same way. By pulling the linear actuator, the biceps and triceps cylinders and muscles act in vice versa. Two different valves are connected to the linear cylinders in order to attach them to a source of liquid and set-up initial pressure of each artificial muscle and initial angular position of the elbow joint (45°). In this mechanical

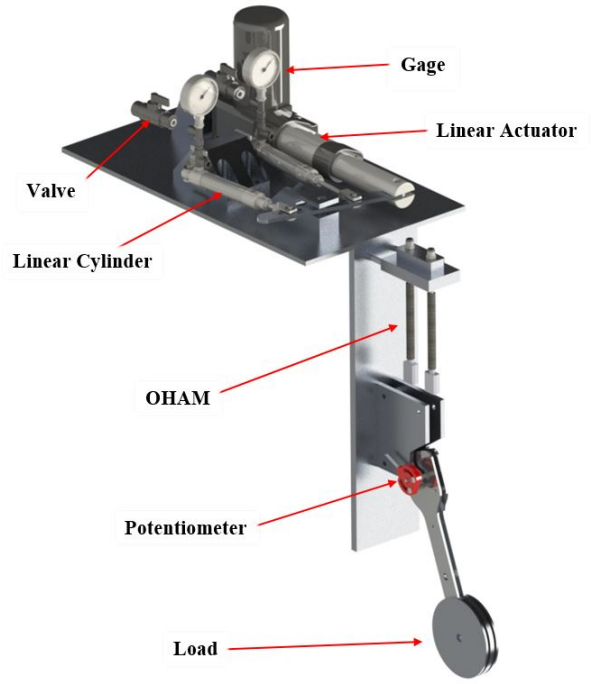

Figure 2.1: Mechanical design of the OHAM platform.

design, common mechanical components in HAMs including servo valves, relief valves, pump, electro-motor, pressure transducer, and source tank have been removed from the mechanical design [76, 44, 73]. Therefore, the weight, volume and total price of actuating system have been decreased. Moreover, the input parameter of the platform is displacement of the linear actuator which provides more accurate position control rather than pressure of the transmission line which is common in control of HAMs. Also, it can be disconnected from the source of fluid after initialization of the angular position of elbow joint which provides a portable system that is necessary for rehabilitation robots. The specification of each component is discussed in the following subsections.

2.1 Linear actuator

The linear actuator is the Deluxe Rod Linear Actuator which is manufactured with a worm gear mechanism to provide quiet and fast operation. This durable and reliable actuator has 3 in. (76.2 mm) stroke and delivers 100 lbf. The specifications of this actuator are shown

in Table 2.1. Also, a schematic view of the liner actuator of the OHAM platform is shown in Figure 2.2.

Table 2.1: The specifications of the linear actuator of the OHAM.

Dynamic Force	100 lbs (444.8 N)
Static Force	180 lbs (800.7 N)
Speed	3 in./second (76.2 mm/s)
Duty Cycle	20%
Stroke Length	3 in. (76.2 mm)
Input	12-volt DC
Max Draw	10 A
Operational Temperature	$-15°$F to $150°$F ($-26°$C to $65°$C)

Figure 2.2: The linear actuator of the OHAM platform.

2.2 Linear cylinders

Two similar linear cylinders from BIMBA company have been used for the OHAM platform. Its piston to rod connection is threaded, sealed, and riveted securely in place with the roll formed rod threads on both ends, and it has the aluminium alloy piston with blow-by flats. Moreover, it has low breakaway with breakaway slots on each end cap for fast seal inflation. The specifications of the cylinders are shown in Table 2.2. Also, a schematic view of the linear cylinder of the OHAM platform is shown in Figure 2.3.

Table 2.2: The specifications of the linear cylinders of the OHAM.

Bore Size	1/4 in. (6.35 mm)
Stroke	1.5 in. (38.1 mm)
Rod Extension	Standard
Pivot Style	Pivot Bushing
Operating Temperature	$-20°$F to 200°F ($-29°$C to $95°$C)
Rod Material	Stainless Steel
Rod End Style	Standard Male Thread

Figure 2.3: The linear cylinder of the OHAM platform.

2.3 Fittings

All connectors of muscles and actuating system are selected similar to each other for consistency and efficiency of the system. Tubing should be inserted into the fittings while an internal gripping ring and O-ring hold the tubing tight. The connectors are also known as instant fittings. For disconnection, the release ring should be pushed on and the tubing needs to be pulled out of the fitting. Also, the fittings have good corrosion resistance which is an important feature for hydraulic systems. The specifications of the fittings are shown in Table 2.3. Fittings of the OHAM platform consist of Barbed Tube Fitting, Push-to-Connect Straight Adapter Tube Fitting and Push-to-Connect Right-Angle Tee Tube Fitting. A schematic view of the fittings of the OHAM platform is shown in Figure 2.4.

Table 2.3: The specifications of the fittings of the OHAM.

Tube Connection Style	Push-to-Connect
O-Ring Material	Buna-N Rubber
Tube Outer Diameter	1/4 in. (6.35 mm)
Pipe Connection Style	1/8 NPT
Tube Connection Material	Nylon Plastic
Pipe Connection Material	Nickel-Plated Brass
Maximum Pressure	290 psi @ 72° F
Operating Temperature	0° F to 170° F

Figure 2.4: Fittings of the OHAM platform. Left: Barbed Tube Fitting, Middle: Push-to-Connect Straight Adapter Tube Fitting, Right: Push-to-Connect Right-Angle Tee Tube Fitting.

2.4 Tubing

A flexible high-pressure nylon tubing has been selected for connection tubes. With slightly softer walls than other hard tubing, this tubing is more flexible and impact absorbent. It is semi-clear, so it provides a limited view of what's flowing through the line which is necessary for hydraulic lines to make sure that no air bubbles are in the line. The specifications of the selected tubing are shown in Table 2.4.

2.5 Sleeving

A fray-resistant expandable sleeving has been selected in order to tighten the rubber tube of the OHAM. Tight braiding makes this sleeving resistant to fraying when cut with scissors which is an essential feature for fabricating artificial muscles. Also, the sleeving is

Table 2.4: The specifications of the tubing of the OHAM.

Hardness	Rockwell R80
Material	Nylon Plastic
Inner Diameter	0.17 in (4.32 mm)
Outer Diameter	1/4 in. (6.35 mm)
Operating Temperature	$-60°$ to $200°$ F
Maximum Pressure	330 psi @ $72°$ F

expandable, so it stretches to fit over the rubber for easy installation, then tightens around its contents for a secure fit. The braided construction permits heat and moisture to dissipate.It is made of polyester, and it resists some wear and chemicals. The specifications of the sleeving are shown in Table 2.5. In the mechanical design of the artificial muscles, uni-

Table 2.5: The specifications of the sleeving of the OHAM.

Sleeving Construction	Tightly Braided
Material	Polyester Fabric
Inner Diameter	1/4 in. (6.35 mm)
Expanded Inner Diameter	7/16 in. (11.11 mm)
Wall Thickness	1/32 in. (0.79 mm)
Operating Temperature	$-90°$ F to $255°$ F
Initial Length	5 in. (127 mm)

form tubing is selected. Based on the outer diameter of tubing, the sleeving of the muscles are selected to fit on the tubing of the artificial muscles which are main components of the OHAMs. the The main components of the OHAMs are shown in Figure 2.5.

Figure 2.5: The main components of the OHAMs. Left: Tubing and Right: Sleeving.

2.6 Oil-Based hydraulic artificial muscles

In order to gain a better understanding of artificial muscles, the OHAMs reported in this work were fabricated in-house utilizing different components and have strokes ranging from 25.4 mm (one inch) to a couple millimetres. The components of one of the custom manufactured OHAMs is shown in Figure 2.6. For the OHAMs, the maximum active length was measured from the inside of top tube clamp to the bottom one when the muscle is fully stretched. All muscles were constructed using the same materials and components for consistency, and experiments were conducted in order to statically characterize the OHAMs. Moreover, all manufactured components of the platform and artificial muscles are made of aluminium alloy due to its advantageous properties (e.g. strength, lightness, corrosion resistance, recyclability and formability).

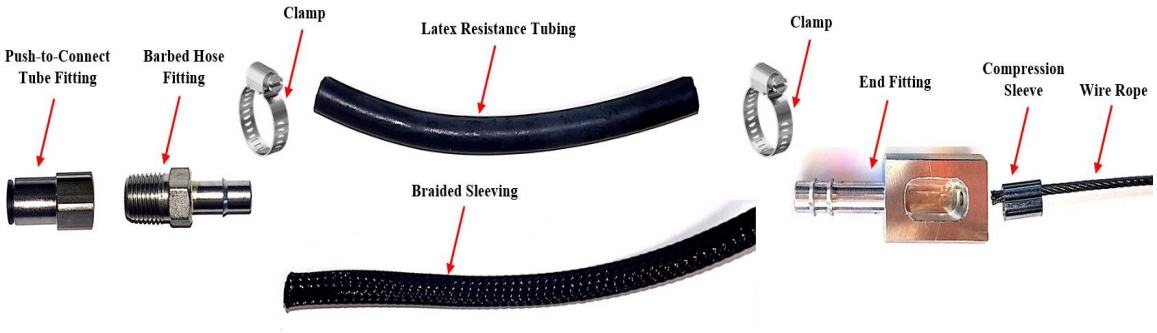

Figure 2.6: The Mechanical components of the OHAM.

Chapter 3

Dynamic modelling

Many theoretical models have been investigated to analyze the properties of artificial muscles. The characteristics of HAMs and PAMs are similar to each other, with some differences in the value of stiffness and damping ratio of the dynamic model. In the history of dynamic modeling of the artificial muscles, different mathematical models have been investigated for PAMs [67, 17, 30]. In general, the dynamic model of HAMs have been determined through two principal methods: phenomenological [29], which is developed experimentally, and energy conservation [8], which is based on the physical geometric analysis of artificial muscles.

3.1 Phenomenological approach

The initial dynamic model for PAMs was developed based on experimental data. The Japanese tire manufacturer Bridgestone presented the use of PAMs for robotic applications [29]. The set-up utilized a pair of PAMs connected by a wire over a pulley to produce rotational motion. The dynamic model used a second order model for the rotation angle of the pulley, with the forcing function proportional to the pressure difference in the actuator pair. The dynamic model did not explicitly present the relationship between friction and the pressure but did give a relationship between contraction force and pressure. The proposed dynamic model was then developed to a two-element passive model [61]. In this dynamic

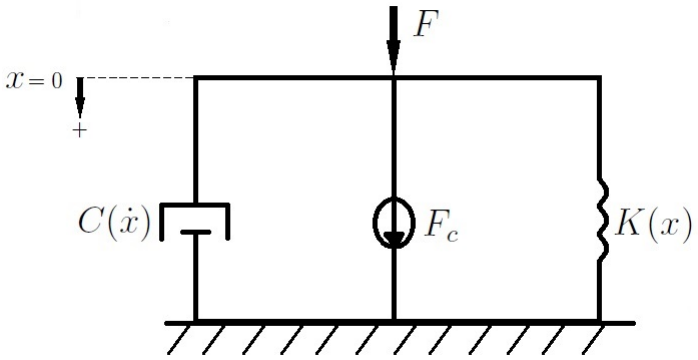

Figure 3.1: The Phenomenological dynamic model to characterize the PAMs.

model, the PAM was suspended vertically with one end fixed rigidly and the other end attached to a mass (M) in order to obtain the parameters of the model. First, the parameters of the spring constant $K(x)$ were determined using steady state force data. Then, the resulting transient force data was used to obtain estimates of the non-linear viscous element $C(\dot{x})$. The Phenomenological dynamic model is shown in Figure 3.1. Subsequently, the proposed dynamic model was further evaluated and parametrised in other studies to develop a robust dynamic model for PAMs [10, 63].

3.2 Energy conservation

In an effort to find the relation between the PAM contraction length, pressure within PAMs, and the actuating force, different research groups applied the principle of virtual work on artificial muscles [12, 7]. With the initial assumption that the PAM maintains its cylindrical shape during inflation and deflation, the principle of virtual work was applied to determine the exerted force. In 1961, Schulte analyzed the relationship between pressure and force and finally represented a model for the behaviour of artificial muscles as shown in Eq. (3.1) [70]. This model reconsidered later by Chou and Hannaford in 1994 in their research [12].

$$F = \frac{\pi D^2 P}{4}[3cos(\lambda)^2 - 1] \tag{3.1}$$

In this static model, F is tensile force, P represents inflation pressure, D is the diameter of the tube, and λ is the angle of fiber. With the assumption that the system is lossless (i.e. no energy is dissipated due to the deformation of the PAM or friction), the energy conservation principle was applied to determine Eq. (3.1). Later in 1996, Chou and Hannaford presented another static model for the behaviour of artificial muscles with assumption that the PAM maintains its cylindrical shape during inflation and deflation utilizing the principle of virtual work. This assumption resulted in a quasi static relation which is shown in Eq. (3.2) [13].

$$F = P\frac{dV}{dL} = P\frac{D_0^2\pi}{4}[\frac{3(1-\epsilon)^2}{\tan^2\alpha_0} - \frac{1}{\sin^2\alpha_0}] \tag{3.2}$$

Where $\epsilon = \frac{L_0 - L}{L_0}$, and the length, diameter and initial pitch angle of the braid of the PAM are L, D and α respectively. The values measured at rest are denoted by the subscript '0', that is when the PAM is fully deflated and the gauge pressure is zero. The Eq. (3.2) shows the change in force exerted by the PAM as it inflates and deflates. At zero contraction the force is maximum and at maximum contraction the force falls to zero. The initial assumptions did not reflect the actual state of the PAM during contraction and resulted in modeling errors. To account for the non cylindrical shape of the inflated PAM, Tondu represented a new model utilizing a correction factor k, where $k \leq 1$, which is added into Eq. (3.2) and resulting in Eq. (3.3) [78].

$$F = P\frac{dV}{dL} = P\frac{D_0^2\pi}{4}[\frac{3(1-k\epsilon)^2}{\tan^2\alpha_0} - \frac{1}{\sin^2\alpha_0}] \tag{3.3}$$

The modified contraction $(k\epsilon)$ is amplified by the factor k. This parameter however, does not modify the maximum force value at zero contraction, since experimentally the PAM does take on a cylindrical shape at zero contraction. Thus the factor k is used to tune the slope of the static model [78].

3.3 OHAM dynamic model

In this work, we have generated a dynamic model of the artificial muscles based on the phenomenological approach. In this model, the dynamic behaviour of artificial muscles consists of a non-linear viscous friction and a non-linear spring which can be determined by experimental tests [63]. The behaviour of the artificial muscles in the inflation and deflation phases is different. Thus, the artificial muscle has been evaluated in both motions to determine the final model. In order to obtain the parameters of the dynamic model, the OHAM was suspended vertically with one end fixed rigidly and the other end was attached to a mass M. First, the spring coefficient $K(x)$ were determined using steady state data. Then, the results from transient condition were used to obtain the viscous element $C(\dot{x})$. The schematic view of OHAM operation with a constant load is shown in Figure 3.2. Where, x is the vertical displacement of the mass M, and $x = 0$ is the position where the artificial muscle is fully deflated. Hence, the resulting equation of motion could be determined as

$$M\ddot{x} + C(\dot{x})\dot{x} + K(x)x = F_c - Mg \tag{3.4}$$

Where, $K(x)$ is the spring coefficient, $C(\dot{x})$ is the damping coefficient, and F_c is the vertical force caused by the contractile element. In the experimental tests, the external force F was due to the weight Mg and inertial load $M\ddot{x}$ of the mass M. Therefore, a dynamic model for a single artificial muscle is determined.

Artificial muscles including PAMs and HAMs are contractile devices. As a result, they can generate forces in only one direction. Therefore, artificial muscles need to be coupled in order to generate bidirectional motion. Opposing pair configuration of artificial muscles have been implemented in different projects, like continuum manipulator [60], Antagonistic Pneumatic Artificial Muscle (APAM) with 1000% elongation capability [82], and a new sleeve PAM in antagonistic configuration with improved performance rather than

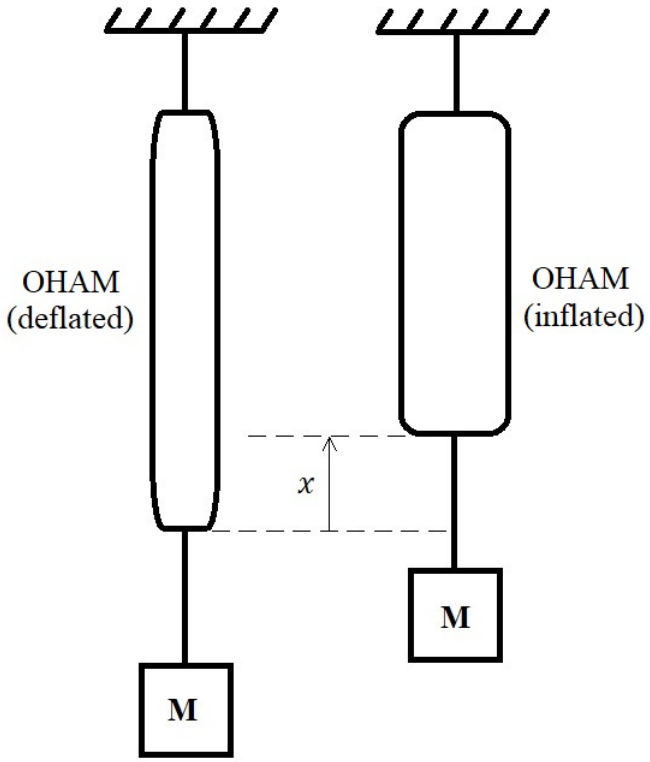

Figure 3.2: The OHAM operation with a constant load.

traditional PAMs [16]. In order to implement human-like muscles, antagonistic set-up of OHAMs should be implemented which mimics skeletal muscles in human body. As one of the muscles (biceps) pulls up the load, the other one (triceps) will act as a brake to stop the load at its threshold position. Also, to push down the load in the opposite direction, the muscles act in the other direction. The antagonistic set-up is generating rotational movements to manipulate different objects in both directions. In this project, we have implemented a new configuration for the elbow joint rather than utilizing pulley mechanism which is common in opposing pair configurations [46, 75, 1, 28]. In this configuration, artificial muscles are connected to the joint in biceps and triceps configuration with 45° deviation from the forearm link in the OHAM platform. As a result, the deviation of artificial muscles is decreased so that the muscle forces are vertical during angular rotation which simplifies the dynamic model of the systems. In the dynamic model, the total force of each OHAM is proportional to the applied pressure by the cylinders which is determined

by the displacement of the linear actuator. In the following subsection, a dynamic model is presented for the OHAM platform in biceps-triceps configuration.

3.4 Biceps-triceps configuration

The schematic of the OHAMs in the antagonistic pair configuration is shown in Figure 3.3. The upper arm is connected to a motionless reference and it remains stationary during contraction and expansion of the artificial muscles. The external load is considered as the weight of an external mass (M_l) which is held at the end of the forearm, and it is adjustable for multiple purposes and various experimental tests. Mass of the forearm (M_f) is considered in the center of mass of the forearm $(L/2)$. Also, a frictionless joint is connecting the upper arm and the forearm of the system. The artificial muscles are attached to the forearm with the same distance to the joint, and they are placed on a circle with a constant radius (r), which is the distance from the joint to the effecting points of the artificial muscles. The forces of the biceps and triceps muscles in inflating position (F_{bi}, F_{ti}) are different from biceps and triceps muscles in deflation position (F_{bd}, F_{td}) due to the characteristics of the artificial muscles. The distance from the center of mass of the load (the shape is disk with radius R) to the joint is considered L. The forearm is free to rotate through an angle θ, where $\theta = -45^\circ$ corresponds to the arm being fully straightened (the mass is in the extreme downward position), and $\theta = 45^\circ$ corresponds to the arm being fully bent (the mass is in the extreme upward position). In the design of the forearm, two factors are considered to simplify the dynamic model of the OHAM system:

- The angle of 45° is considered in the design of the forearm, where the effecting point of the artificial muscles in the forearm have the same height from the joint and they are vertical in the workspace of the elbow joint. As a result, the artificial muscles have minimum deviation during angular rotations and forces caused by artificial muscles act almost vertically (less than 2°).

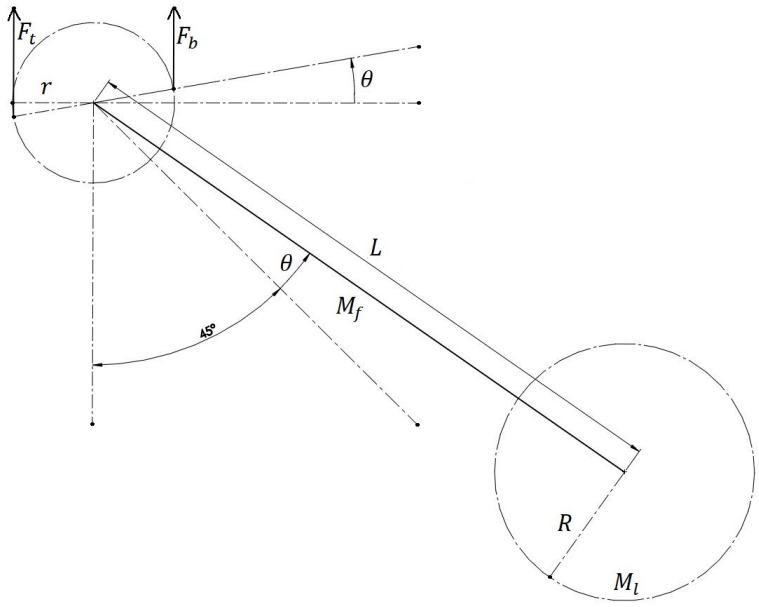

Figure 3.3: Dynamic modeling of the OHAM platform in the biceps-triceps configuration.

- The forearm consists of two plates which are connected with round standoffs in the effecting points of the artificial muscles in the forearm, and corrosion-resistant wire rope (316 stainless steel) is looped with compression sleeve (18-8 Stainless Steel). As a result, the wire rope does not have contact with the joint (unlike pulley) which minimizes the friction of the system.

In Eq. (3.5), the dynamic model of the OHAM system is presented utilizing Newton's Second Law ($\sum_{i=1}^{n} M_i = I\ddot{\theta}$).

$$I\ddot{\theta} = -M_l g L \sin(\frac{\pi}{4} + \theta) - M_f g \frac{L}{2} \sin(\frac{\pi}{4} + \theta) - F_t r \cos(\theta) + F_b r \cos(\theta) \tag{3.5}$$

where, $M_l g L \sin(\frac{\pi}{4}+\theta)$ and $M_f g \frac{L}{2} \sin(\frac{\pi}{4}+\theta)$ are clockwise torques imparted to the forearm by the acceleration of gravity (g) from the disk and forearm respectively. Since the lifting force exerted by a single OHAM on the forearm is determined in Eq. (3.4), the biceps and triceps forces in counter clockwise rotation are determined in Eqs. (3.6) and (3.7) respectively.

$$F_b = F_{cb} - C_i(\dot{x})\dot{x} - K_i(x)x \tag{3.6}$$

$$F_t = F_{ct} + C_d(\dot{x})\dot{x} + K_d(x)x \tag{3.7}$$

So, the counter clockwise biceps torque and clockwise triceps torque are $F_b r\cos(\theta)$ and $F_t r\cos(\theta)$ respectively, and F_{cb} and F_{ct} are the vertical forces caused by the contractile element in biceps and triceps artificial muscles respectively. The stiffness and damping coefficients of the artificial muscles in biceps and triceps configuration have different values during inflation and deflation motions. Based on previous system identifications [63, 61] and our experimental tests, the stiffness and damping coefficients of the artificial muscles are shown in Eq. (3.8) in which a_i, a'_i, b_i and b'_i are constant parameters. In the following equations, i and d represent inflation and deflation conditions respectively.

$$\begin{aligned} K_i(x) &= a_2x^2 + a_1x + a_0 \\ K_d(x) &= a'_2x^2 + a'_1x + a'_0 \\ C_i(\dot{x}) &= b_2\dot{x}^2 + b_1\dot{x} + b_0 \\ C_d(\dot{x}) &= b'_2\dot{x}^2 + b'_1\dot{x} + b'_0 \end{aligned} \tag{3.8}$$

It is important to note that the coefficients of Eq. (3.8) vary with the driven mass and the state of the system [61]. They can be reduced to only four fixed second order polynomials corresponding to the inflation and deflation states. For example, the stiffness of a single HAM in the inflation motion is determined as $K_i(x) = 0.8614x^2 - 2.483x + 3.1702$ with $R^2 = 0.9345$. The most important thing about Eq. (3.8) is that the coefficients will be bounded in the workspace of the elbow joint (fully strengthened to fully bent) which is essential for the non-linear control of the artificial muscles. In the dynamic model, the biceps and triceps forces affect at the same time. Based on the elbow angle, the biceps and triceps forces have different values. We define the following parameters, to simplify the dynamic equation as given in Eq. (3.9).

$$\begin{aligned} U &= F_{ct} - F_{cb} \\ K(x) &= K_i(x) + K_d(x) \\ C(\dot{x}) &= C_i(\dot{x}) + C_d(\dot{x}) \end{aligned} \tag{3.9}$$

The coefficients corresponding to these elements (K, C, and U) depend on the input pressure P supplied to the HAMs. In most PAM platforms, the pressure is commanded externally by adjusting the voltage supplied to the inlet valve. In this work, the pressure is commanded by varying the voltage supplied to the linear actuator which provides rotation in the rocking arm. To activate the flexion, timed pressure pulses can be used which are electrically controlled by the driver of the linear actuator. To activate the extension of the elbow joint, inflation of triceps artificial muscle can be accomplished via opposing actuation with the linear actuator in the system. In order to simplify the last two terms in Eq. (3.5), we need to determine $F_b - F_t$. Substituting parameters defined in Eq. (3.9) into Eqs. (3.6) and (3.7), $F_b - F_t$ can be determined as follows:

$$F_b - F_t = -U - C(\dot{x})\dot{x} - K(x)x \tag{3.10}$$

Substituting Eq. (3.10) into Eq. (3.5), we can rewrite Eq. (3.5) in terms of U, $K(x)$, and $C(\dot{x})$ as follows:

$$I\ddot{\theta} = -M_l g L \sin(\frac{\pi}{4} + \theta) - M_f g \frac{L}{2} \sin(\frac{\pi}{4} + \theta) - [U + C(\dot{x})\dot{x} + K(x)x] r \cos(\theta) \tag{3.11}$$

In Eq. (3.11), x and $\dot{x}$ are displacement and velocity of the artificial muscles. As $x = r\sin(\theta)$ and $\dot{x} = r\dot{\theta}\cos(\theta)$, we can rewrite Eq. (3.11) by replacing x and $\dot{x}$ in $K(x)x$ and $C(\dot{x})\dot{x}$ respectively. Therefore, we can rewrite Eq. (3.11) entirely in terms of θ and $\dot{\theta}$ as given in Eq. (3.12):

$$I\ddot{\theta} = -[M_l g L + M_f g \frac{L}{2}] \sin(\frac{\pi}{4} + \theta) - U r \cos(\theta) - r^2 C(\dot{\theta})\dot{\theta} \cos^2(\theta) - r^2 K(\theta) \sin(\theta) \cos(\theta) \tag{3.12}$$

Also, I is the moment of inertia of the forearm and disk about the elbow joint which is calculated in Eq. (3.13).

$$I = I_f + I_l = (\frac{1}{3} M_f L^2) + (\frac{1}{2} M_l R^2 + M_l L^2) \tag{3.13}$$

The input of the system is U, which is determined by how much the artificial muscle is inflated. Note that the whole system in triceps lifting and biceps lifting conditions is controllable for all values of θ. Since the force exerted by the artificial muscles are always multiplied by $\cos(\theta)$, the system for $\theta = -45^\circ$ to $\theta = 45^\circ$, which covers the elbow rotation from fully strengthened to fully bent, is controllable and the elbow joint angle could reach its thresholds.

Chapter 4

Control

The major challenge inherent in presenting a controller for artificial muscles is the non-linear characteristics of muscles. Many non-linear control theories have been presented for artificial muscles, including adaptive tracking [40], adaptive neural network [64], and sliding mode tracking [41]. Also, the backstepping controller is presented for a single muscle in previous projects [10]. The implementation of control methods on artificial muscles have been presented by some research groups, like model-based feedforward control [44], PI feedback control of a Manipulator Arm [72] and cascade control [86]. In this project, an integrator backstepping controller is presented for artificial muscles in an opposing pair configuration.

4.1 Background

4.1.1 Open-Loop

The simplest control method to be discussed is open-loop control. In this method, no signals are fed back into the control system and it is developed based on the dynamic model of the platform to generate proper results. Open-loop control method can successfully be implemented in simple and accurate plants that do not require precise control. In the history of the control of artificial muscles, some research groups have implemented open-loop control methods in their platforms. For example, a research group has implemented a

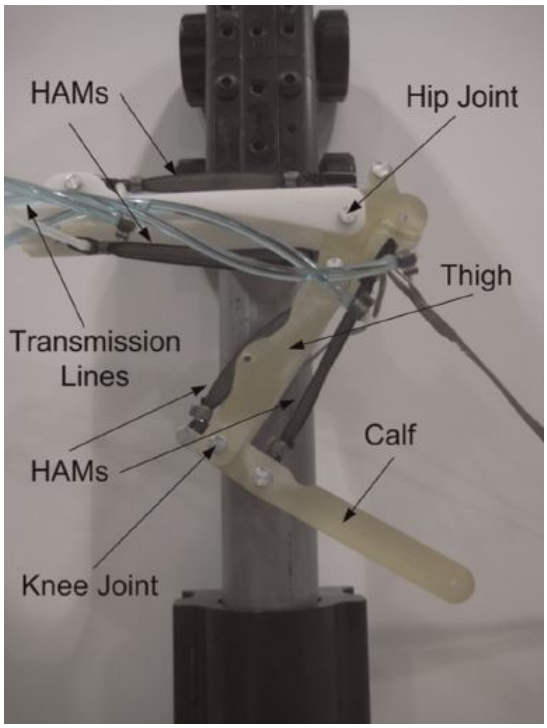

Figure 4.1: Schematic of a 2-DOF leg test rig with HAMs utilizing open-loop control strategy [76].

two-Degree-of-Freedom (2-DOF) leg test rig with HAMs [76] as shown in Figure 4.1.

4.1.2 Pole placement

Another control Strategy is the pole placement technique, where the position of control system's poles are chosen to obtain desired performance. Pole placement control uses state feedback to generate the corresponding input. Different research projects have implemented the pole placement technique to control PAMs. In 1994, adaptive pole placement controllers were applied to control a reference trajectory. Accuracies of 1° were reported for constant set-points; however, the system response was very slow [7]. In 1996, adaptive pole-placement techniques were again applied to control joint angle utilizing a PID controller. Position accuracy of ± 5 degrees was presented at pressures up to 800 kPa [27].

4.1.3 PID control

The most common control strategy for artificial muscles is PID control. A Proportional (P) controller changes the output that is proportional to the current error value and decrease rise time and steady state error; however, it causes small changes in the settling time and increases the overshoot of the system. An Integral (I) controller accumulates the error over time, multiplies it by an integral gain, and adds the result to the controller output. This gain decreases rise time and steady state error; however, it increases the settling time and overshoot of the system. A Derivative (D) controller multiplies the rate of change of the error by a derivative gain which decreases the rate of change of the controller output along with the overshoot of the system; however, it causes small changes in settling time and overshoot of the system. Many research groups have implemented different combination of P, I and D controllers in their system [57, 14, 81, 15]. Recently, new combination of PID control methods with other control strategies have been presented by some research groups, like model-based feedforward control [44], PI feedback control of a Manipulator Arm [72] and cascade control [86]. A 10-DOF exoskeleton robot with PAMs utilizing PID control strategy is shown in Figure 4.2.

4.1.4 Fuzzy control

Another control strategy to be discussed is fuzzy control. Fuzzy control can be used to overcome models with different uncertainties, because it provides a way to determine a definite conclusion using vague, ambiguous, imprecise, noisy, or missing input information. The Fuzzy approach is not mathematical but it mimics how a person would make decisions. This method is proposed by Lotfi A. Zadeh in 1965 [87, 88] and the Fuzzy controller has been implemented in various artificial muscle platforms [11, 2] recently.

Figure 4.2: Schematic of a 10-DOF exoskeleton robot with PAMs utilizing PID control strategy [15].

4.1.5 Adaptive control

Another advanced control strategy is adaptive control. This method modifies the controller over time in order to adapt time-varying system parameters or disturbances. In 2007, a research group developed a non-linear pressure observer based adaptive robust controller. The pressure observer was used to estimate unknown pressures while the adaptive robust controller effectively attenuated uncertainties. Experiments in that platform expressed that the plant had good control accuracy and smooth trajectories [2]. Another research is independent joint position and stiffness adaptive control on a manipulator consisting of an agonist-antagonist pair of pneumatic artificial muscles connected by a cable around a pulley [79]. Simulations showed that adaptive control can cope with model uncertainties more rigorous, and presents better tracking performance rather than PID control. Figure 4.3 shows a 1-DOF link actuated by a pair of McKibben artificial muscles in antagonist con-

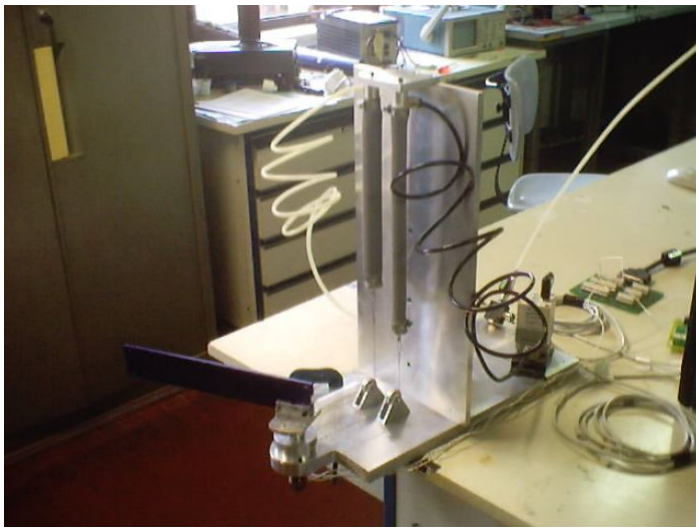

Figure 4.3: Schematic of a 1-DOF link actuated by a pair of McKibben artificial muscles in antagonist configuration utilizing adaptive control strategy. [79].

figuration utilizing adaptive control strategy [79].

4.1.6 Neural networks

One of the new control strategies is neural networks which is inspired by human brain. One of the examples is implementation of a non-linear PID control with neural networks for position control of a simulated three-link manipulator driven by PAMs. The controller parameters were adapted iteratively within the neural network utilizing the input and output of the plant and the conventional backpropagation algorithm. The PID gains were non-linear functions of error and were adapted utilizing the Steepest Descent Method (SDM). Consequently, the PID controller with neural networks performed more stronger than a conventional PID control [75]. Another research is a joint angle position controller for a manipulator driven by PAMs. In this project, an adaptive neural network controller updated the weights of the manipulator's inverse characteristics and applied them to the inverse dynamic model in order to obtain an appropriate voltage control signal. Simulations indicated that the applied controller was superior to a conventional PID controller [1].

4.1.7 Impedance control

The next control strategy to be discussed is impedance control which is used to control the dynamic interaction between a robotic manipulator and its environment. Impedance control was not used to track position or force trajectories. It attempts to tune mechanical impedance according to a specified purpose and the appropriate impedance depends on the application of the manipulators. Impedance control is appropriate for robots that must interact with humans because there is a need to control the interaction between the robotic manipulator and the human [27]. An example of this method is implementation of an impedance control strategy in a PAM rehabilitation robot. In this project, mechanical impedance of the human arm was used as a tool to assess the physical condition of the applicant so that impedance parameters of the controller could be modified appropriately [57]. Another example is the development of powered exoskeletons driven by PAMs for upper and lower body rehabilitation. An impedance control scheme provided the execution of advanced resistive motions. Impedance control was used when the robot was interacting with the human, particularly during operational training when the human was trying to eat or grasp selected objects [9].

4.1.8 Model predictive control

The last control strategy, Model Predictive Control (MPC), is a method often used in process control. It uses a model of the process to predict future outputs and attempts to bring the predicted output as close as possible to the reference trajectory by minimizing an error function between the reference and predicted output. For instance, a research group implemented model predictive control to control two sets of PAMs driving a high speed linear axis [69]. A schematic of their test platform is shown in Figure 4.4.

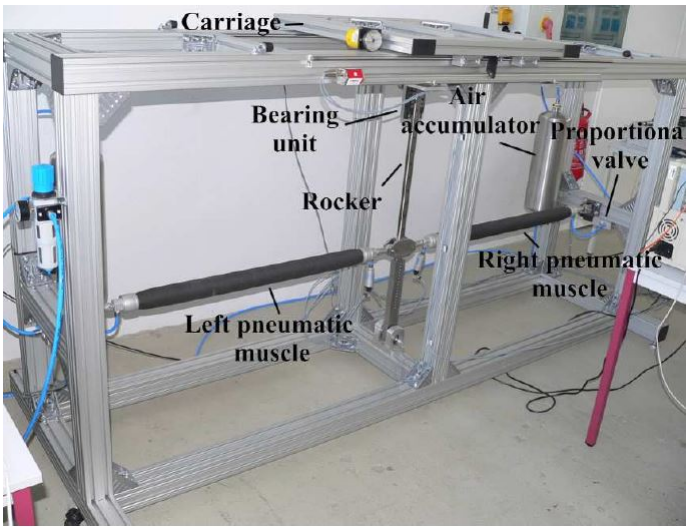

Figure 4.4: Schematic of a high speed linear axis actuated by two sets of PAMs utilizing model predictive control strategy [69].

4.2 Backstepping control

In the field of control systems, backstepping control is a technique developed in 1992 by Petar V. Kokotovic [38] and others [42] for designing stabilizing controllers for strict-feedback systems that are also known as ”lower triangular”. A typical feedback linearization approach in most cases leads to cancellation of some non-linearities. The backstepping design, however, exhibits more flexibility in comparison to feedback linearization, since it does not need the resulting input or output dynamics be linear [34]. The selected systems are built from subsystems that can be stabilized using some other methods. Due to the recursive structure of the subsystems, the designer can start the controller design process at the known-stable system and develop new controllers that progressively stabilize the other subsystem. The process terminates when the last control is reached. Hence, this process is known as backstepping [34]. The backstepping approach provides a recursive method for stabilizing the origin of a system in strict-feedback form. That is, consider a system of the

form

$$\begin{cases} \dot{x} & = f_x(x) + g_x(x)z_1 \\ \dot{z}_1 & = f_1(x, z_1) + g_1(x, z_1)z_2 \\ \dot{z}_2 & = f_2(x, z_1, z_2) + g_2(x, z_1, z_2)z_3 \\ \vdots & \\ \dot{z}_k & = f_k(x, z_1, z_2, \ldots, z_k) + g_k(x, z_1, z_2, \ldots, z_k)u \end{cases} \tag{4.1}$$

where

- $x \in \mathbb{R}$ with $N \geq 1$,
- $z_1, z_2, \ldots, z_k$ are scalars,
- u is a scalar input to the system,
- $f_x, f_1, f_2, \ldots, f_k$ vanish at the origin (i.e. $f_i(0, 0, \ldots, 0) = 0$)
- $g_x, g_1, g_2, \ldots, g_k$ are non-zero over the domain of interest (i.e. $g_i(0, 0, \ldots, 0) \neq 0$ for $1 \leq i \leq k$)

Also assume that the subsystem

$$\dot{x} = f_x(x) + g_x(x)u_x(x) \tag{4.2}$$

is stabilized to the origin by some known control $u_x(x)$ such that $u_x(0) = 0$. It is also assumed that a Lyapunov function $V(x)$ for this stable subsystem is known. That is , this x subsystem is stabilized by some other methods and backstepping extends its stability to the z shell around it. The backstepping approach determines how to stabilize the x subsystem using z_1, and then proceeds with determining how to make the next state z_2 drive z_1 to the control required to stabilize x. Thus, the process "steps backward" from x out of the strict-feedback form system until the ultimate control u is designed. Hence, Backstepping provides a way to extend the controlled stability of this subsystem to the larger system. A control $u_1(x, z_1)$ is designed so that the system

$$\dot{z}_1 = f_1(x, z_1) + g_1(x, z_1)u_1(x, z_1) \tag{4.3}$$

is stabilized so that z_1 follows the desired u_x control. The control design is based on the augmented Lyapunov function candidate

$$V_1(x, z_1) = V_x(x) + \frac{1}{2}(z_1 - u_x(x))^2 \tag{4.4}$$

The control u_1 can be picked to bound $\dot{V}_1$, so that this process continues until the actual u is known, and the real control u stabilizes z_k to fictitious control u_{k-1}, the fictitious control u_1 stabilizes z_1 to fictitious control u_x, and the fictitious control u_x stabilizes x to the origin. This process is known as backstepping because it starts with the requirements on some internal subsystem for stability and progressively steps back out of the system, maintaining stability at each step. Because

- f_i vanish at the origin for $0 \leq i \leq k$,
- g_i are non-zero for $1 \leq i \leq k$
- the given control u_x has $u_x(0) = 0$

then the resulting system has an equilibrium at the origin (i.e., where $x = 0$, $z_1 = 0$, $z_2 = 0$,..., and $z_k = 0$) that is globally asymptotically stable.

4.3 Integrator-backstepping control

In this section, we present the derivation of our control approach, based on the non-linear controller design technique known as integrator-backstepping controller. By reducing the order of Eq. (3.12) into two first-order differential equations, the state-space representation of the system can be determined. Thus, we can solve the differential equations utilizing Ordinary Differential Equation (ODE) solvers in MATLAB software. The ODE solvers implement the Runge-Kutta method which is suited for solving ODEs by predictions. In Eq. (4.5), the state-space model of our OHAM system is presented in which x_1 and x_2

are state variables and represent θ (angular position) and $\dot{\theta}$ (angular velocity) of the system respectively.

$$\begin{aligned}
\dot{x_1} &= x_2 \\
\dot{x_2} &= -[\frac{M_l g L + M_f g \frac{L}{2}}{I}] \sin(\frac{\pi}{4} + x_1) - \frac{r^2}{I} C(x_2) x_2 \cos^2(x_1) - \frac{r^2}{I} K(x_1) \sin(x_1) \cos(x_1) \\
&\quad - U \frac{r}{I} \cos(x_1)
\end{aligned} \tag{4.5}$$

In the integrator-backstepping controller [33], a stabilizing control can be found for a system in the form of Eq. (4.6).

$$\begin{aligned}
\dot{x_1} &= f_1(x_1) + g_1(x_1) x_2 \\
\dot{x_2} &= f_2(x_1, x_2) + g_2(x_1, x_2) U
\end{aligned} \tag{4.6}$$

Where x_1 and x_2 are state variables and U is the control input of the system. In HAM pair configurations, we have $f_1(x_1) = 0$ and $g_1(x_1) = 1$. Based on the design and dynamic model of HAMs, they typically have different $f_2(x_1, x_2)$ and $g_2(x_1, x_2)$. A block diagram of the state-space model of the HAMs in opposing-pair configuration is shown in Figure 4.5. In our OHAM platform, the gain of the system is equal to one and $f_2(x_1, x_2)$ and $g_2(x_1, x_2)$ are defined in Eqs. (4.7) and (4.8) respectively.

$$\begin{aligned}
f_2(x_1, x_2) = -[\frac{M_l g L + M_f g \frac{L}{2}}{I}] \sin(\frac{\pi}{4} + x_1) - \frac{r^2}{I} C(x_2) x_2 \cos^2(x_1) \\
- \frac{r^2}{I} K(x_1) \sin(x_1) \cos(x_1)
\end{aligned} \tag{4.7}$$

$$g_2(x_1, x_2) = -\frac{r}{I} \cos(x_1) \tag{4.8}$$

Also, we define a new variable U' as shown in Eq. (4.9).

$$U = \frac{1}{g_2(x_1, x_2)} [U' - f_2(x_1, x_2)] \tag{4.9}$$

As a result, we can rewrite Eq. (4.6) as shown in Eq. (4.10).

$$\begin{aligned}
\dot{x_1} &= x_2 \\
\dot{x_2} &= U'
\end{aligned} \tag{4.10}$$

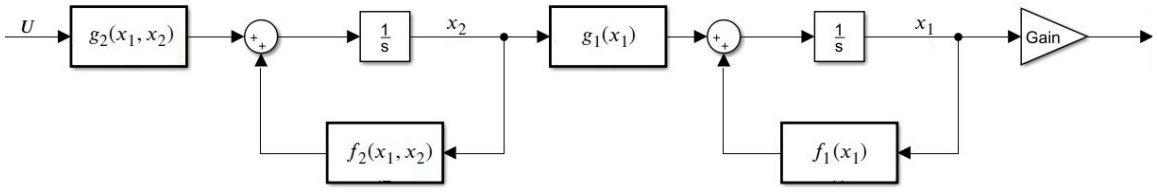

Figure 4.5: Block diagram of the state-space model of the HAMs in an antagonistic pair configuration.

A tracking error variable is defined as $e = x_1 - x_{1d}$. Its derivative, taking into account Eq. (4.10), is determined to be $\dot{e} = x_2 - \dot{x}_{1d}$ where x_{1d}, $\dot{x}_{1d}$, and $\ddot{x}_{1d}$ are assumed known and bounded. So, we can rewrite Eq. (4.10) as follows

$$\begin{aligned} \dot{e} &= x_2 - \dot{x}_{1d} \\ \dot{x}_2 &= U' \end{aligned} \tag{4.11}$$

The stabilizing control law is presented by x_{2d}. Based on integrator-backstepping concept, we define an independent input x_{2d} as shown in Eq. (4.12) so that it provides stability requirement of the $\dot{e}$ in Eq. (4.11) by choosing a proper Lyapunov function.

$$x_{2d} = \frac{1}{g_1(x_1)}[-e + \dot{x}_{1d} - f_1(x_1)] = -e + \dot{x}_{1d} \tag{4.12}$$

Choosing the Lyapunov function $V_1 = \frac{1}{2}e^2$, the $\dot{V}_1$ is determined in Eq. (4.13) where $\dot{V}_1 < 0$ for all $e \neq 0$.

$$\dot{V}_1 = e\dot{e} = e(-e) = -e^2 \tag{4.13}$$

An error variable is defined as $z = x_2 - x_{2d}$. Its derivative is determined to be

$$\dot{z} = \dot{x}_2 - \dot{x}_{2d} \tag{4.14}$$

Where $\dot{x}_2 = U'$ and $\dot{x}_{2d} = -\dot{e} + \ddot{x}_{1d}$. So, we can rewrite Eq. (4.11) and present the non-linear system utilizing the new variables in Eq. (4.15).

$$\begin{aligned} \dot{e} &= z - e \\ \dot{z} &= U' + z - e - \ddot{x}_{1d} \end{aligned} \tag{4.15}$$

The Lyapunov function candidate for Eq. (4.15) is chosen to be

$$V_2(e, z) = V_1(e) + \frac{1}{2}z^2 \tag{4.16}$$

and its time derivative is determined as

$$\dot{V}_2 = e\dot{e} + z\dot{z} = e(z - e) + z(U' + z - e - \ddot{x}_{1d}) = -e^2 + z(U' + z - \ddot{x}_{1d}) \tag{4.17}$$

by choosing $U' = -Nz + \ddot{x}_{1d}$ for all $N > 1$, the time derivative of V_2 is determined in Eq. (4.18) where $\dot{V}_2 < 0$ for all $e \neq 0$ and $z \neq 0$, and the OHAM system is globally asymptotically stable for e and z variables.

$$\dot{V}_2 = -e^2 - z^2(N - 1) \tag{4.18}$$

Since $e = x_1 - x_{1d}$ and $z = x_2 - x_{2d}$, we can rewrite the input signal of the OHAM system utilizing x_1, x_2 and x_{1d} variables

$$U' = -N(x_2 + x_1 - x_{1d} - \dot{x}_{1d}) + \ddot{x}_{1d} \tag{4.19}$$

Where U' is defined in Eq. (4.9) and we can rewrite control input of the OHAM system as follows

$$U = \frac{1}{g_2(x_1, x_2)}[-N(x_2 + x_1 - x_{1d} - \dot{x}_{1d}) + \ddot{x}_{1d} - f_2(x_1, x_2)] \tag{4.20}$$

where $f_2(x_1, x_2)$ and $g_2(x_1, x_2)$ are defined in Eq. (4.7), and they can be different functions based on the dynamic model of the HAMs. Therefore, Eq. (4.20) presents a backstepping non-linear controller for HAMs with non-linear uncertainties and the system is globally asymptotically stable for x_1 and x_2 variables. Consequently, the integrator-backstepping controller for our OHAM system is determined in Eq. (4.21).

$$\begin{aligned} U = \frac{1}{-\frac{r}{I}\cos(x_1)}[-N(x_2 + x_1 - x_{1d} - \dot{x}_{1d}) + \ddot{x}_{1d} + [\frac{M_l g L + M_f g \frac{L}{2}}{I}]\sin(\frac{\pi}{4} + x_1) \\ + \frac{r^2}{I}C(x_2)x_2\cos^2(x_1) + \frac{r^2}{I}K(x_1)\sin(x_1)\cos(x_1) \end{aligned} \tag{4.21}$$

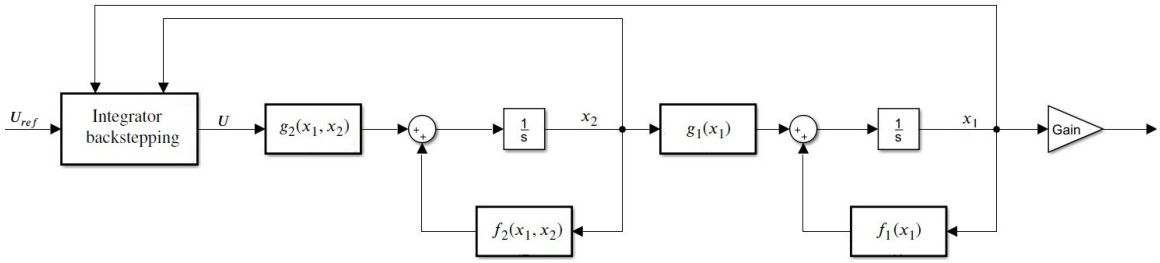

Figure 4.6: Block diagram of the HAMs in an antagonistic pair configuration utilizing integrator-backstepping controller.

By picking large enough feedback N gain, the ultimate bound for the error variable $z = x_2 - x_{2d}$ can be rendered arbitrarily small. The block diagram of the HAMs in opposing-pair configuration utilizing integrator-backstepping controller is shown in Figure 4.6 [54].

Chapter 5

Implementation and discussion

In this chapter, we present the apparatus of the OHAM platform and implementation process of the OHAMs in an antagonistic configurations. Moreover, we discuss the experimental tests of the applied Integrator-backstepping Controller along with the advantages and disadvantages of the proposed platform in comparison to other existing platforms.

5.1 Apparatus of the OHAM platform

The schematic of the mechanical components of the OHAMs and its hydraulic systems are shown in Figure 5.1. The test platform is used to determine the characteristics of the OHAMs and evaluate the control algorithm. The signal analysis and experimental tests are implemented in National Instrument LabVIEW software [5, 53]. The signal process-

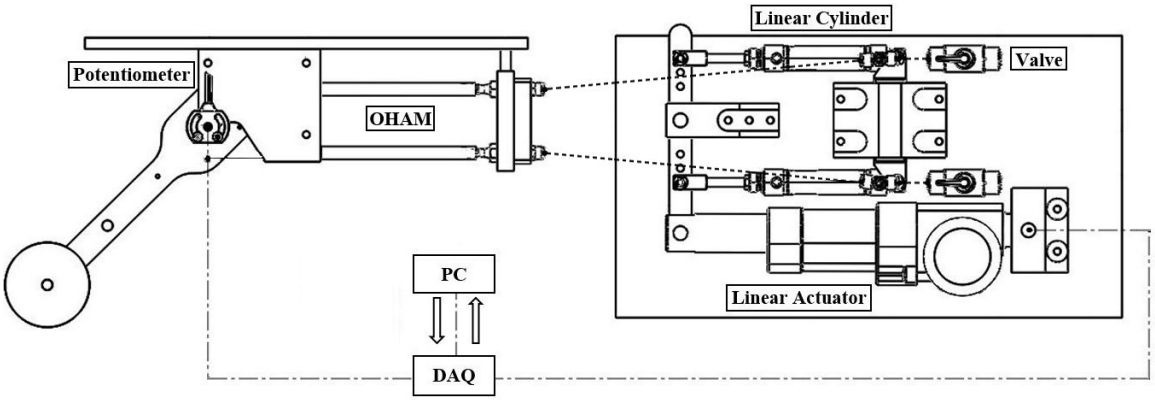

Figure 5.1: Diagram of the elbow joint, OHAMs and hydraulic system (hydraulic transmission lines in a single dashed line and electrical signals in a double dashed line).

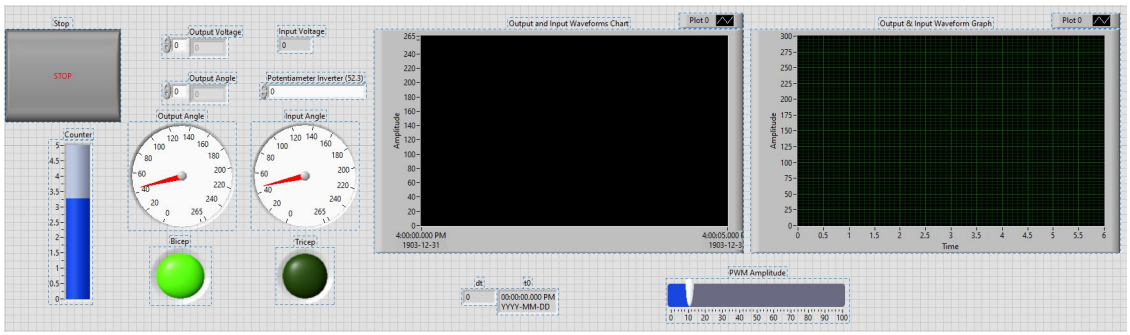

Figure 5.2: The front panel of the LabVIEW program of the OHAM platform.

ing of the system is implemented in USB-6221 Multifunctional I/O Device from National Instrument. It has 16 AI (16-Bit, 250 kS/s), 2 AO (833 kS/s), and 24 DIO USB Multifunction I/O which offers analogue I/O, correlated digital I/O, two 32-bit counters/timers, and digital triggering which provides high resolution and different filtering features for online implementations [35]. The front panel of the LabVIEW program of the OHAM platform is shown in Figure 5.2.

The online desired input angle of elbow joint is entered into LabVIEW software. The output angle of the system is measured by an angular potentiometer, with 250 degrees of adjustment, and acts as a feedback sensor in the system in order to measure the angular position of the elbow joint. In order to measure the output angle, the inner part of the potentiometer is fixed to the motionless shaft, and the outer part of the potentiometer is attached to the forearm. Two phases of motion for the muscles are considered as follows:

- If the input angle is more than the output angle of the elbow joint, the linear actuator will compress its piston. As a result, the biceps cylinder will be pressurized and then the biceps muscle will be inflated, and the elbow joint will lift the forearm in flexion.

- If the input angle is less than the output angle of the elbow joint, the linear actuator will expand its piston. As a result, the triceps cylinder will be pressurized and then the triceps muscle will be inflated, and the elbow joint will lower the forearm in extension.

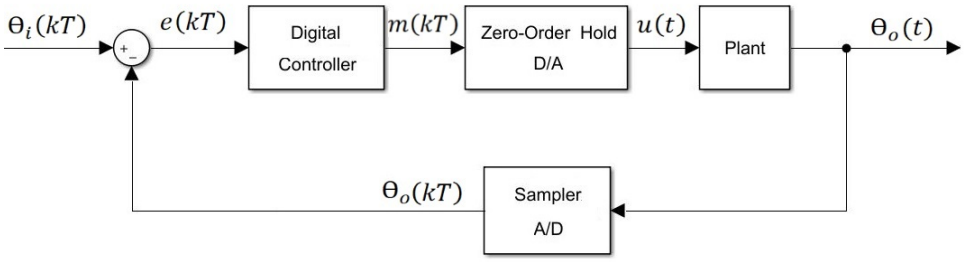

Figure 5.3: Block diagram of the OHAM platform utilizing PID controller.

This motion will be continued until the difference between the input angle and the output angle becomes zero. As the system is non-linear, the elbow angle has oscillation in first experimental tests specially in high frequencies (more than 0.5 Hz). By the implementation of a manually tuned PID controller to the system in the LabVIEW program, the bouncing is removed, and the system performs better than an open-loop system. In terms of consistency in the results of this research, $r = 0.5\,in\,(12.7mm)$, $R = 2\,in\,(50.8mm)$, $L = 8\,in\,(203.2mm)$, $M_f = 0.4\,lb\,(181.4g)$, and $M_l = 2.7\,lb\,(1224.7g)$ in all experimental tests. The block diagram of the PID controller for elbow joint is shown in Figure 5.3. Where the sampler, A/D converter, digital controller, zero-order hold, and D/A converter produce a continuous-time control signal $u(t)$ to be fed to the plant. In the system, the output signal $\theta_o(t)$ is received from the potentiometer, and it is converted to digital signal using DAQ. It is then fed back for comparison with input signal $\theta_i(t)$ which is entered through LabVIEW program. The digital error signal $e(kT) = \theta_i(kT) - \theta_o(kT)$ is fed to digital controller, which operates on the sampled sequence $e(kT)$ to produce the signal $m(kT)$. The digital PID controller is tuned manually in order to remove the bouncing of the output angle. The experimental apparatus of the OHAM platform is shown in Figure 5.4.

5.2 Experimental tests

In the experimental tests, angular position of the input and output angles of the elbow joint are recorded. Then, the input and output data are analyzed by System Identification Tool-

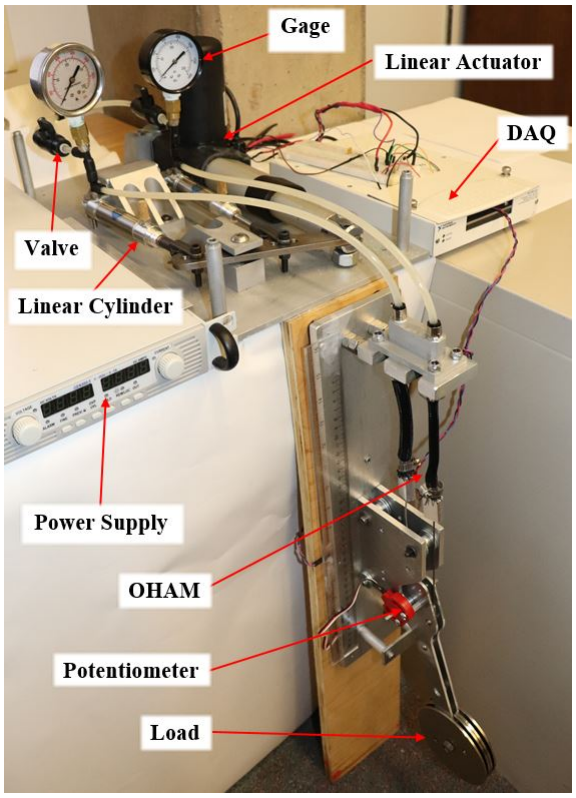

Figure 5.4: The experimental apparatus of the OHAM platform.

box of the MATLAB software in order to determine the characteristics of the real system. We have identified different linear and non-linear models for the response of our system with different accuracies in comparison to experimental outputs. The accuracy of the best linear model was 94.37%, and the accuracy of the best non-linear model was 95.40%. The experimental input angles, the experimental output angles and the most accurate linear simulated model of the step input are shown in Figure 5.5. It validates that the simplifications in the dynamic modeling are acceptable for the system, because the accuracy difference is almost 1%. It would be better to mention that higher accuracy of the human-like motion would be achieved if stronger OHAMs were implemented in the platform. Consequently, experimental results from system identification are implemented in control algorithm for tracking experimental tests. Consequently, the transfer function of the system can be determined using MATLAB software. Based on the specifications that can be selected in the

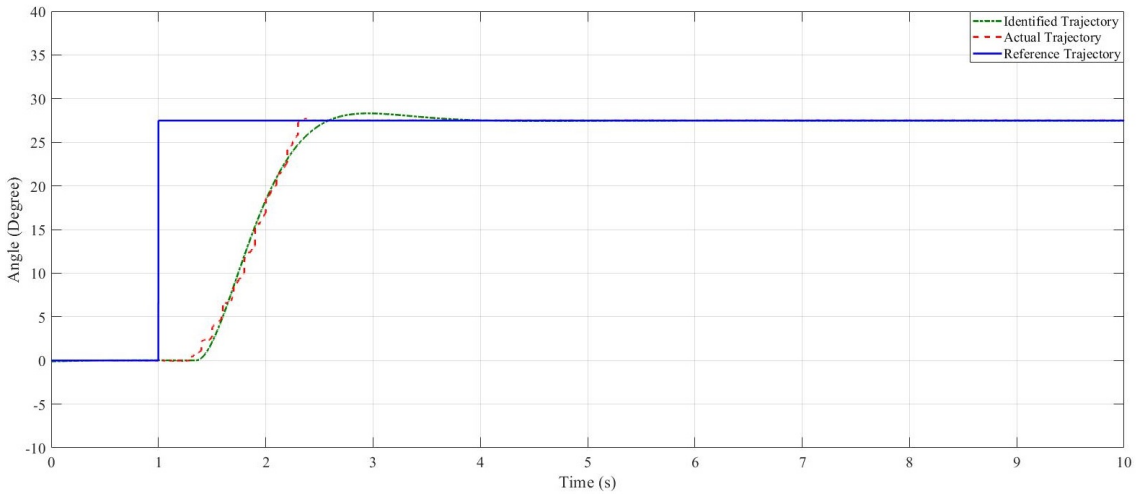

Figure 5.5: System identification results of the OHAM platform (reference trajectory in a blue line, actual trajectory in a red single dashed line and identified trajectory in a green double dashed line).

system identification toolbox, different transfer functions with various characteristics can be presented for the system. For example, a second order system with two poles and zero zeros without delay has been selected for system identification and the result is presented in Eq. (5.1). It should be noted that the accuracy of this model is 94.37%.

$$G(s) = \frac{2.8828}{s^2 + 0.9634s + 3.3839} \tag{5.1}$$

During experimental tests, different ranges of motion and frequencies of the sinusoidal references are selected to qualify the proposed models and muscles. Figure 5.6 and Figure 5.7 show the results of the sinusoidal trajectory tracking at frequency of 0.1 Hz and 0.2 Hz respectively. In these figures, the reference trajectory is the desired input angle (x_{1d}) which is entered online into the LabVIEW software, and the actual trajectory is the output angle (x_1) which is measured experimentally utilizing an angular potentiometer. Also, the error of the system is defined as the difference between the reference trajectory and the actual trajectory. The maximum error of the system between reference trajectory and actual trajectory are 1.77° and 3.08° for the amplitude of 20° and frequency of 0.1 Hz

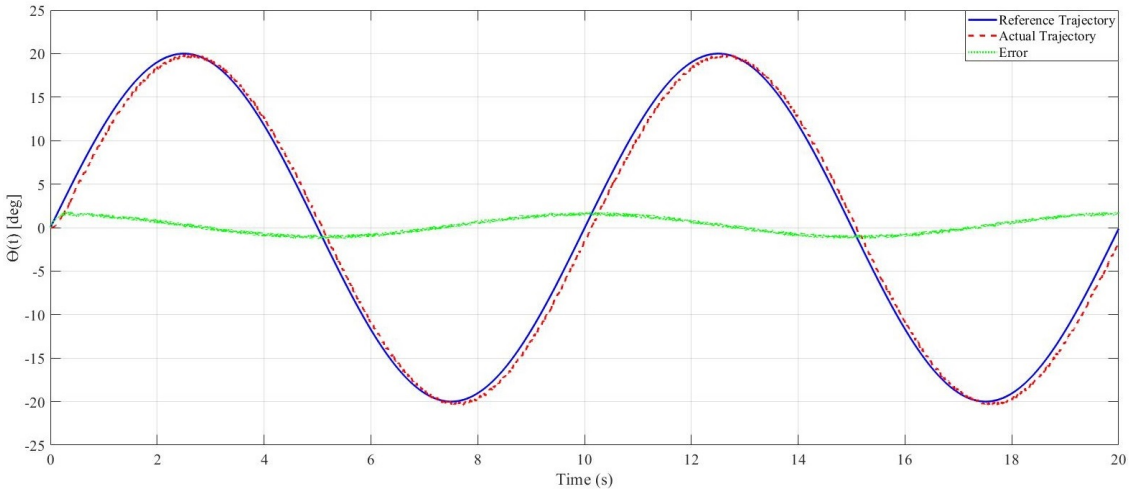

Figure 5.6: Tracking of sinusoidal trajectory with amplitude range of $40°$ and frequency of 0.1 Hz. (reference trajectory in a blue line, measured trajectory in a red single dashed line and error angle in a green dotted line)

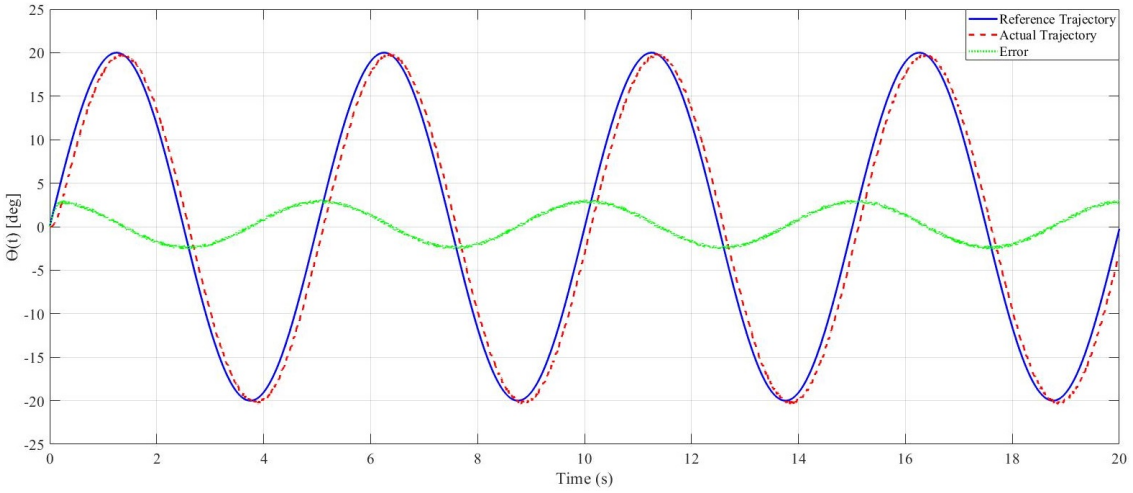

Figure 5.7: Tracking of sinusoidal trajectory with amplitude range of $40°$ and frequency of 0.2 Hz (reference trajectory in a blue line, measured trajectory in a red single dashed line and error angle in a green dotted line).

and 0.2 Hz respectively. The aforementioned results show that the platform can perform motion tracking with acceptable accuracy. However, in higher frequencies the accuracy of the platform should be improved. It should be noted that higher frequencies would be achieved if we had used stronger artificial muscles instead of custom manufactured artificial muscles. For instance, the materials that have used for the sleeving and tubing of the custom manufactured artificial muscles didn't work properly in higher frequencies (more than 1 Hz) and caused damage to artificial muscles. Therefore, the accuracy of the presented integrator-backstepping controller should not decrease in higher frequencies. The performance achieved by the proposed controller can be compared with related approaches in the scientific literature on control of hydraulic muscle actuators in an antagonistic pair configuration. In [85], a PID control approach is applied on a system with combined pneumatic/hydraulic mode operation; a maximum joint error of 15° is achieved for a reference trajectory with a range of 40° (maximum error of 37.5%) and a frequency of 0.1 Hz. In [37], an MPC controller with RLS approach is implemented on water hydraulic muscle actuator; a maximum displacement error is decreased from 22.5 mm to 5.55 mm for a sinusoidal reference trajectory with an amplitude of 20° (maximum error of 13.875%) and frequency of 0.1 Hz. In [73], a sliding mode impedance control is tested on a hydraulic muscle actuator; a maximum error of 1.21 mm is achieved for a sinusoidal reference trajectory with an amplitude of 6.4 mm (maximum error of 9.453%) and frequency of 0.25 Hz. It has improved common issues with sliding mode control strategies (e.g. slow response and lack of robustness). Also, it shows a maximum error of 0.786 mm for a square-like continuous reference trajectory with a lower bound of 6.4 mm and upper bound of 19 mm (maximum error of 6.238%). In [44], a cascaded PI-P control with feedforward is tested on six parallel HAMs; a maximum error is decreased to less than 1° for a sinusoidal reference trajectory with maximum range of 10° (maximum error of less than 10%) and frequency of 0.25 Hz. It is important to mention that controller analysis that is discussed for simi-

lar projects doesn't prove which controller is more accurate due to different specifications of the mechanical components of the platforms and corresponding artificial muscles (e.g. length of HAMs, number of HAMs, diameter of HAMs, pressure range, material of sleeving, material of tubing, weight of the system, etc.) that affect the performance of the HAM platforms. But, the functionality of our control method and the OHAM system is confirmed for the case of sinusoid reference tracking with different frequency ranges up to 0.2 Hz. Moreover, the control algorithm can be implemented at higher frequencies with various mechanical specifications. The experimental results prove that the proposed control algorithm for pneumatic/hydraulic artificial muscles in an antagonistic pair configuration provides acceptable tracking response which is necessary for rehabilitation purposes. Also, our platform yields accurate tracking performance in comparison with similar platforms in the field of control of HAMs in an antagonistic pair configuration. Additionally, we have evaluated the performance of the Integrator-backstepping controller for the HAMs in an antagonistic pair configuration by comparing the performance of the Integrator-backstepping controller with a PID controller as shown in Figure 5.8. It should be pointed out that the PID gains are manually tuned, and its accuracy can be slightly improved; however, we tried to remove oscillations to avoid physical damages to the system. Indeed, the PID control is barely stable and its tracking performance is poor, despite exhaustive trial and error determination of the optimal PID gains. The results demonstrate the importance of applying advanced control techniques along with the PID controllers commonly used in PAM and HAM research studies [46, 44, 86].

5.3 Highlights and challenges

The main advantage of our platform is that common mechanical components for actuating artificial muscles (e.g. servo valve, relief valve, filters, pump, electro-motor, pressure transducer and tank) have been replaced by a linear actuator, two cylinders and two me-

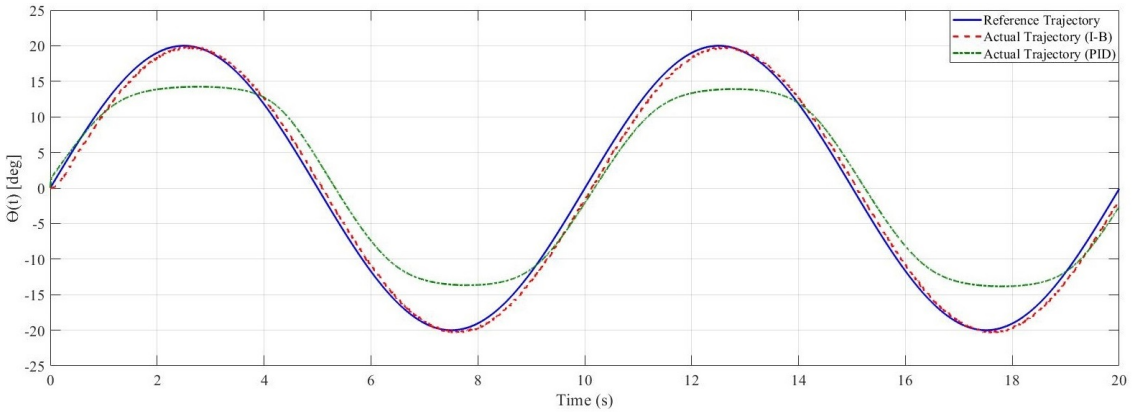

Figure 5.8: Tracking performance comparison of sinusoidal trajectory with amplitude range of 40° and frequency of 0.1 Hz between Integrator-backstepping controller and PID controller (reference trajectory in a blue line, measured trajectory of Integrator-backstepping controller in a red single dashed line, and measured trajectory of PID controller in a green double dashed line).

chanical valves which makes the platform simple for empirical investigations. Also, the system can be disconnected from the source of fluid which provides the potential for a portable system. Moreover, HAMs are using oil which consumes less energy than air for operating the elbow joint along with removing common limitations of water-based systems (e.g. corrosion, filtering, and low boiling point). The main drawback of the platform is that custom artificial muscles are implemented in the system which makes it difficult to accurately compare the functionality of the platform with other existing platforms. Another drawback of the system is that oil has higher flammability, and its spills result in slip safety hazards and is less environmentally friendly than water or air common in artificial muscles [58]. Another advantage of the system is that the dynamic model is presented for an antagonistic pair (biceps-triceps) configuration for actuating an elbow joint. This modeling is based on a phenomenological approach and can be implemented in different projects with various artificial muscles. However, developing other approaches for dynamic modeling of the platform would increase the accuracy of the system. Another advantage of this work is the presentation of an integrator-backstepping controller for HAMs and PAMs in an opposing-pair configuration which can be used for different systems with various stiffness

and damping coefficients. Implementation of other advanced control methods might have better responses and higher accuracies for our platform; however, our intent is to explore and implement novel control strategies for HAMs in an antagonistic pair configuration which has not been discussed in detail. Some research groups have shown the effectiveness of integrator-backstepping controller for a single PAM [10, 62], but it needs more empirical investigations for bidirectional artificial muscles.

Chapter 6

Conclusions

6.1 Results

This work introduces a new OHAM test platform, utilizing an antagonistic muscle pair. The detailed mechanical design of the test platform was presented along with the specifications of an OHAM. A detailed dynamic model was determined for OHAM system platform to actuate an artificial elbow joint. Moreover, an integrator-backstepping controller was developed for HAMs in an antagonistic pair configuration which can be used for different systems with various functions and specifications. From the experimental tests of the feedback position control of the OHAMs, it was validated that proposed platform, artificial muscles and integrator-backstepping controller presented in this work can be implemented for the control of different system plants.

6.2 Future Work

In the future of this project, experimental tests of different non-linear controllers will be compared for the OHAM platform. Moreover, the input angle of the system will be replaced by an inertia measurement unit (IMU) or Electromyography (EMG) sensors in order to receive input signals directly from human muscles. Therefore, it could be implemented as a wearable rehabilitation robotic platform in near future. In addition, other

joints could be added to current system in order to increase number of active joints and develop a human-like arm actuated with hydraulic artificial muscles.

Appendix A

In the following figures, we have added detailed specifications of the mechanical components of the OHAM platform along with the schematic of the corresponding part.

Female Threaded Round Standoff

18-8 Stainless Steel, 1/4" OD, 1/4" Long, 8-32 Thread Size

Shape	Round
Material	18-8 Stainless Steel
OD	1/4"
OD Tolerance	-0.005" to 0.005"
Length	1/4"
Length Tolerance	-0.005" to 0.005"
Thread Size	8-32
Threading	Fully Threaded
Thread Length	1/4"
Gender	Female
Thread Fit	Class 2B
Tensile Strength	80,000 psi
Hardness	Rockwell B60
System of Measurement	Inch
Specifications Met	ASTM A581 or A582
RoHS	RoHS 3 (2015/863/EU) Compliant
REACH	REACH (EC 1907/2006) (01/16/2020, 205 SVHC) Compliant
Country of Origin	United States

Figure 6.1: Female threaded round standoff

Push-to-Connect Tube Fitting

Straight Adapter, for 1/4" Tube OD x 1/8 NPT Female

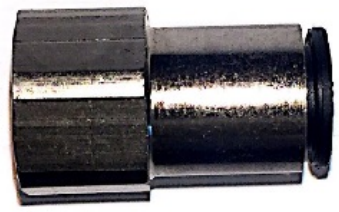

Shape	Straight
Type	Adapter
For Use With	Air, Water, Oil
Tube Connection	
Connection Style	Push to Connect
Push-to-Connect Type	Standard
Gender	Female
O-Ring Material	Buna-N Rubber
For Tube OD	1/4"
Pipe Connection	
Connection Style	Threaded
Gender	Female
Thread Type	NPT
Pipe Size	1/8
Material	Nickel-Plated Brass
Release Type	Ring
Release Ring	
Material	Plastic
Color	Black
Maximum Pressure	290 psi @ 72° F
Maximum Vacuum	28 in. of Hg @ 72° F
Vacuum Rating	Standard
Temperature Range	0° to 170° F
Length	63/64"
For Tube	
Material	Polyethylene Plastic, Polyurethane Rubber
Hardness Rating	Firm
Hardness	Durometer 95A-45D
Specifications Met	ISO 14743
RoHS	RoHS 3 (2015/863/EU) compliant with exemption 6(c) - Lead in copper alloy
REACH	Not Compliant
Country of Origin	Mexico

Figure 6.2: Push-to-connect tube fitting (Straight)

Stainless Steel High-Pressure Barbed Tube Fitting

for Air and Water, for 1/4" Tube ID x 1/8 NPT Male

Shape	Straight
Type	Adapter
For Use With	Air, Water, Oil
Tube Connection	
Connection Style	Barbed
Barbed Connection Type	Clamp On
Barb Style	Standard
Number of Barbs	Single
Gender	Male
For Tube ID	1/4"
Pipe Connection	
Connection Style	Threaded
Gender	Male
Thread Type	NPT
Pipe Size	1/8
Material	303 Stainless Steel
Maximum Pressure	250 psi @ 72° F
Maximum Vacuum	27 in. of Hg @ 72° F
Vacuum Rating	Standard
Temperature Range	-40° to 1200° F
Length	1 1/32"
Sterilize With	Ethylene Oxide, Radiation, Steam (Autoclaving)
For Tube	
Material	EVA Plastic, Polyethylene Plastic, Polypropylene Plastic, PVC Plastic
Hardness Rating	Firm
Hardness	Durometer 75A-95A
RoHS	RoHS 3 (2015/863/EU) Compliant
REACH	REACH (EC 1907/2006) (01/16/2020, 205 SVHC) Compliant
Country of Origin	United States

Figure 6.3: Stainless steel high-pressure barbed tube fitting

Corrosion-Resistant Wire Rope

Not for Lifting, 316 Stainless Steel, 7 x 7, 1/16" Diameter

Application	Not for Lifting
Attachment Type	Plain
Diameter	1/16"
Capacity	70 lbs.
Recommended Pulley/Drum Diameter	2 5/8"
Material	316 Stainless Steel
Finish	Unfinished
Wire Rope Coating	Uncoated
Construction	7 x 7
Flexibility	Flexible
Core Type	Strand
Lubrication	Lubricated
Preformed	Yes
RoHS	RoHS 3 (2015/863/EU) Compliant
REACH	REACH (EC 1907/2006) (01/16/2020, 205 SVHC) Compliant
Country of Origin	United States

Figure 6.4: Corrosion-resistant wire rope

Push-to-Connect Tube Fitting

Right-Angle Tee, for 1/4" Tube OD x 1/8 NPT Male

Shape	Tee
Type	Adapter
Tee Style	Right Angle
For Use With	Air, Water, Oil
Tube Connection	
Connection Style	Push to Connect
Push-to-Connect Type	Standard
Gender	Female
O-Ring Material	Buna-N Rubber
For Tube OD	1/4"
Pipe Connection	
Connection Style	Threaded
Gender	Male
Thread Type	NPT
Pipe Size	1/8
Tube Connection Material	Nylon Plastic
Pipe Connection Material	Nickel-Plated Brass
Color	Black
Clarity	Opaque
Release Type	Ring
Release Ring Material	Plastic
Release Ring Color	Black
Maximum Pressure	290 psi @ 72° F
Maximum Vacuum	28 in. of Hg @ 72° F
Vacuum Rating	Standard
Temperature Range	0° to 170° F
For Tube	
Material	Polyethylene Plastic, Polyurethane Rubber
Hardness Rating	Firm
Hardness	Durometer 95A-45D
Specifications Met	ISO 14743
Swivel Type	Intermittent
Features	PTFE Thread Sealant
RoHS	RoHS 3 (2015/863/EU) compliant with exemption 6(c) - Lead in copper alloy
REACH	Not Compliant
Country of Origin	Mexico

Figure 6.5: Push-to-connect tube fitting (Tee)

Wire Rope Compression Sleeve - for Lifting

for Steel Rope, Zinc-Plated Copper, for 1/16" Rope Diameter

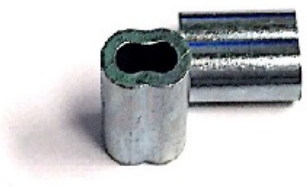

Fitting Type	Compression Sleeve
Application	For Lifting
Material	Zinc-Plated Copper
For Wire Rope Material	Steel
For Wire Rope	
Diameter	1/16"
Construction	7 × 7 Strand Core 7 × 19 IWRC 7 × 19 Strand Core
Attachment Type	Loop
Sleeve Length	3/8"
Required Installation Tool	Compression Tool
Required Number of Compressions	1
Capacity	100% of the Rope's Capacity
Specifications Met	ASME B30.9, MS51844
RoHS	RoHS 3 (2015/863/EU) Compliant
REACH	REACH (EC 1907/2006) (01/16/2020, 205 SVHC) Compliant
Country of Origin	United States

Figure 6.6: Wire-rope compression sleeve

Bibliography

[1] K. K. Ahn and H. P. H. Anh. Design and implementation of an adaptive recurrent neural networks (ARNN) controller of the pneumatic artificial muscle (PAM) manipulator. *Mechatronics*, 19(6):816–828, 2009.

[2] K. Balasubramanian and K. S. Rattan. Trajectory tracking control of a pneumatic muscle system using fuzzy logic. In *NAFIPS 2005-2005 Annual Meeting of the North American Fuzzy Information Processing Society*, pages 472–477. IEEE, 2005.

[3] K. Berns, J. Albiez, V. Kepplin, and C. Hillenbrand. Airbug—insect-like machine actuated by fluidic muscle. In *4th International Conference on Climbing and Walking Robots*, pages 237–244, 2001.

[4] A. M. Bertetto and M. Ruggiu. Characterization and modeling of air muscles. *Mechanics Research Communications*, 31(2):185–194, 2004.

[5] R. H. Bishop. *LabVIEW 8*. Pearson, 2007.

[6] D. Büchler, H. Ott, and J. Peters. A lightweight robotic arm with pneumatic muscles for robot learning. In *2016 IEEE International Conference on Robotics and Automation (ICRA)*, pages 4086–4092. IEEE, 2016.

[7] D. G. Caldwell, G. A. Medrano-Cerda, and M. Goodwin. Characteristics and adaptive control of pneumatic muscle actuators for a robotic elbow. In *Proceedings of the 1994*

IEEE international conference on robotics and automation, pages 3558–3563. IEEE, 1994.

[8] D. G. Caldwell, G. A. Medrano-Cerda, and M. Goodwin. Control of pneumatic muscle actuators. *IEEE Control Systems Magazine*, 15(1):40–48, 1995.

[9] D. G. Caldwell, N. G. Tsagarakis, S. Kousidou, N. Costa, and I. Sarakoglou. "soft" exoskeleton for upper and lower body rehabiliation-desing, control and testing. *International Journal of Humanoid Robotics*, 4(03):549–573, 2007.

[10] P. Carbonell, Z.-P. Jiang, and D. Repperger. Nonlinear control of a pneumatic muscle actuator: backstepping vs. sliding-mode. In *Proceedings of the 2001 IEEE International Conference on Control Applications (CCA'01)(Cat. No. 01CH37204)*, pages 167–172. IEEE, 2001.

[11] X. Chang and J. H. Lilly. Fuzzy control for pneumatic muscle tracking via evolutionary tuning. *Intelligent Automation & Soft Computing*, 9(4):227–244, 2003.

[12] C.-P. Chou and B. Hannaford. Static and dynamic characteristics of mckibben pneumatic artificial muscles. In *Proceedings of the 1994 IEEE international conference on robotics and automation*, pages 281–286. IEEE, 1994.

[13] C.-P. Chou and B. Hannaford. Measurement and modeling of mckibben pneumatic artificial muscles. *IEEE Transactions on robotics and automation*, 12(1):90–102, 1996.

[14] R. W. Colbrunn, G. M. Nelson, and R. D. Quinn. Design and control of a robotic leg with braided pneumatic actuators. In *Proceedings 2001 IEEE/RSJ International Conference on Intelligent Robots and Systems. Expanding the Societal Role of Robotics in the the Next Millennium (Cat. No. 01CH37180)*, volume 2, pages 992–998. IEEE, 2001.

[15] N. Costa and D. G. Caldwell. Control of a biomimetic" soft-actuated" 10dof lower body exoskeleton. In *The First IEEE/RAS-EMBS International Conference on Biomedical Robotics and Biomechatronics, 2006. BioRob 2006.*, pages 495–501. IEEE, 2006.

[16] M. F. Cullinan, C. McGinn, and K. Kelly. Sleeve Pneumatic Artificial Muscles for Antagonistically Actuated Joints. In *2019 International Conference on Robotics and Automation (ICRA)*, pages 8360–8366. IEEE, 2019.

[17] L. Cveticanin, M. Zukovic, I. Biro, and J. Sarosi. Mathematical investigation of the stability condition and steady state position of a pneumatic artificial muscle–mass system. *Mechanism and Machine Theory*, 125:196–206, 2018.

[18] F. Daerden, D. Lefeber, et al. Pneumatic artificial muscles: actuators for robotics and automation. *European journal of mechanical and environmental engineering*, 47(1):11–21, 2002.

[19] D. P. Ferris, J. M. Czerniecki, and B. Hannaford. An ankle-foot orthosis powered by artificial pneumatic muscles. *Journal of applied biomechanics*, 21(2):189–197, 2005.

[20] Festo. Festo company, 2020.

[21] M. Focchi, E. Guglielmino, C. Semini, A. Parmiggiani, N. Tsagarakis, B. Vanderborght, and D. G. Caldwell. Water/air performance analysis of a fluidic muscle. In *2010 IEEE/RSJ International Conference on Intelligent Robots and Systems*, pages 2194–2199. IEEE, 2010.

[22] S. Ganguly, A. Garg, A. Pasricha, and S. Dwivedy. Control of pneumatic artificial muscle system through experimental modelling. *Mechatronics*, 22(8):1135–1147, 2012.

[23] H. F. George and A. Barber. What is bulk modulus and when is it important. *Hydraulics & Pneumatics*, 7:34–39, 2007.

[24] N. Goulbourne. A mathematical model for cylindrical, fiber reinforced electro-pneumatic actuators. *International Journal of Solids and Structures*, 46(5):1043–1052, 2009.

[25] B. Hannaford and J. Winters. Actuator properties and movement control: biological and technological models. In *Multiple muscle systems*, pages 101–120. Springer, 1990.

[26] T. Hesselroth, K. Sarkar, P. P. Van Der Smagt, and K. Schulten. Neural network control of a pneumatic robot arm. *IEEE Transactions on Systems, Man, and Cybernetics*, 24(1):28–38, 1994.

[27] N. Hogan. Impedance control: An approach to manipulation. In *1984 American control conference*, pages 304–313. IEEE, 1984.

[28] A. Hošovskỳ, J. Pitel', K. Židek, M. Tóthová, J. Sárosi, and L. Cveticanin. Dynamic characterization and simulation of two-link soft robot arm with pneumatic muscles. *Mechanism and Machine Theory*, 103:98–116, 2016.

[29] K. Inoue. Rubbertuators and applications for robots. In *Proceedings of the 4th international symposium on Robotics Research*, pages 57–63, 1988.

[30] B. Kalita and S. Dwivedy. Nonlinear dynamics of a parametrically excited pneumatic artificial muscle (pam) actuator with simultaneous resonance condition. *Mechanism and Machine Theory*, 135:281–297, 2019.

[31] K. Kawamura, R. A. Peters, D. M. Wilkes, W. A. Alford, and T. E. Rogers. ISAC: Foundations in human-humanoid interaction. *IEEE Intelligent Systems and their Applications*, 15(4):38–45, 2000.

[32] K. Kawashima, T. Sasaki, A. Ohkubo, T. Miyata, and T. Kagawa. Application of robot arm using fiber knitted type pneumatic artificial rubber muscles. In *IEEE International Conference on Robotics and Automation, 2004. Proceedings. ICRA'04. 2004*, volume 5, pages 4937–4942. IEEE, 2004.

[33] H. K. Khalil. *Nonlinear Systems*. 1996.

[34] H. K. Khalil and J. W. Grizzle. *Nonlinear systems*, volume 3. Prentice hall Upper Saddle River, NJ, 2002.

[35] J. P. King, L. E. Valle, N. Pol, and Y.-L. Park. Design, modeling, and control of pneumatic artificial muscles with integrated soft sensing. In *2017 IEEE International Conference on Robotics and Automation (ICRA)*, pages 4985–4990. IEEE, 2017.

[36] H. Kobayashi and K. Hiramatsu. Development of muscle suit for upper limb. In *IEEE International Conference on Robotics and Automation, 2004. Proceedings. ICRA'04. 2004*, volume 3, pages 2480–2485. IEEE, 2004.

[37] W. Kobayashi, K. Ito, and S.-i. Yamamoto. Displacement control of water hydraulic McKibben muscles with load compensation. *JFPS International Journal of Fluid Power System*, 8(2):107–112, 2014.

[38] P. V. Kokotovic. The joy of feedback: nonlinear and adaptive. *IEEE Control Systems Magazine*, 12(3):7–17, 1992.

[39] K. K. Ku, R. Bradbeer, K. Lam, and L. Yeung. Exploration for novel uses of air muscles as hydraulic muscles for underwater actuator. In *OCEANS 2008-MTS/IEEE Kobe Techno-Ocean*, pages 1–6. IEEE, 2008.

[40] J. H. Lilly. Adaptive tracking for pneumatic muscle actuators in bicep and tricep configurations. *IEEE Transactions on Neural systems and rehabilitation engineering*, 11(3):333–339, 2003.

[41] J. H. Lilly and L. Yang. Sliding mode tracking for pneumatic muscle actuators in opposing pair configuration. *IEEE transactions on control systems technology*, 13(4):550–558, 2005.

[42] R. Lozano and B. Brogliato. Adaptive control of robot manipulators with flexible joints. *IEEE Transactions on Automatic Control*, 37(2):174–181, 1992.

[43] M. Meller, J. Chipka, A. Volkov, M. Bryant, and E. Garcia. Improving actuation efficiency through variable recruitment hydraulic McKibben muscles: modeling, orderly recruitment control, and experiments. *Bioinspiration & biomimetics*, 11(6):065004, 2016.

[44] M. Meller, B. Kogan, M. Bryant, and E. Garcia. Model-based feedforward and cascade control of hydraulic McKibben muscles. *Sensors and Actuators A: Physical*, 275:88–98, 2018.

[45] M. A. Meller, M. Bryant, and E. Garcia. Reconsidering the McKibben muscle: Energetics, operating fluid, and bladder material. *Journal of Intelligent Material Systems and Structures*, 25(18):2276–2293, 2014.

[46] A. Merola, D. Colacino, C. Cosentino, and F. Amato. Model-based tracking control design, implementation of embedded digital controller and testing of a biomechatronic device for robotic rehabilitation. *Mechatronics*, 52:70–77, 2018.

[47] T. V. Minh, B. Kamers, H. Ramon, and H. Van Brussel. Modeling and control of a pneumatic artificial muscle manipulator joint–part i: Modeling of a pneumatic artificial muscle manipulator joint with accounting for creep effect. *Mechatronics*, 22(7):923–933, 2012.

[48] T. V. Minh, T. Tjahjowidodo, H. Ramon, and H. Van Brussel. Cascade position control of a single pneumatic artificial muscle–mass system with hysteresis compensation. *Mechatronics*, 20(3):402–414, 2010.

[49] T. Nakamura and H. Shinohara. Position and force control based on mathematical models of pneumatic artificial muscles reinforced by straight glass fibers. In *Proceedings 2007 IEEE International Conference on Robotics and Automation*, pages 4361–4366. IEEE, 2007.

[50] V. L. Nickel, J. Perry, and A. L. Garrett. Development of useful function in the severely paralyzed hand. *JBJS*, 45(5):933–952, 1963.

[51] R. Niiyama, A. Nagakubo, Y. Kuniyoshi, et al. A bipedal jumping and landing robot with an artificial musculoskeletal system. in robotics and automation. In *IEEE International Conference on. 2007.*, 2007.

[52] R. Niiyama, S. Nishikawa, and Y. Kuniyoshi. Athlete robot with applied human muscle activation patterns for bipedal running. In *2010 10th IEEE-RAS International Conference on Humanoid Robots*, pages 498–503. IEEE, 2010.

[53] A. Nikkhah and C. Bradley. Implementation of Oil-Based Hydraulic Artificial Muscles in a Bio-inspired Configuration. In *2019 IEEE Pacific Rim Conference on Communications, Computers and Signal Processing (PACRIM)*, pages 1–5. IEEE, 2019.

[54] A. Nikkhah, C. Bradley, and A. S. Ahmadian. Design, dynamic modeling, control and implementation of hydraulic artificial muscles in an antagonistic pair configuration. *Mechanism and Machine Theory*, 153:104007, 2020.

[55] A. Nikkhah, H. Keshavarz, A. Yousefi-Koma, and S. S. Mohtasebi. Design, dynamic modeling and fabrication of a bio-inspired quadruped robot. In *2015 3rd RSI International Conference on Robotics and Mechatronics (ICROM)*, pages 593–599. IEEE, 2015.

[56] A. Nikkhah, A. Yousefi-Koma, R. Mirjalili, and H. M. Farimani. Design and implementation of small-sized 3d printed surena-mini humanoid platform. In *2017 5th RSI International Conference on Robotics and Mechatronics (ICRoM)*, pages 132–137. IEEE, 2017.

[57] T. Noritsugu and T. Tanaka. Application of rubber artificial muscle manipulator as a rehabilitation robot. *IEEE/ASME Transactions On Mechatronics*, 2(4):259–267, 1997.

[58] A. Parr. *Hydraulics and pneumatics: a technician's and engineer's guide*. Elsevier, 2011.

[59] Y. Peng, Y. Liu, Y. Yang, N. Liu, Y. Sun, Y. Liu, H. Pu, S. Xie, and J. Luo. Development of continuum manipulator actuated by thin McKibben pneumatic artificial muscle. *Mechatronics*, 60:56–65, 2019.

[60] M. B. Pritts and C. D. Rahn. Design of an artificial muscle continuum robot. In *IEEE International Conference on Robotics and Automation, 2004. Proceedings. ICRA'04. 2004*, volume 5, pages 4742–4746. IEEE, 2004.

[61] D. Repperger, K. Johnson, and C. Phillips. A VSC position tracking system involving a large scale pneumatic muscle actuator. In *Proceedings of the 37th IEEE conference*

on decision and control (Cat. No. 98CH36171), volume 4, pages 4302–4307. IEEE, 1998.

[62] W. T. Reutzel and C. D. Rahn. Adaptive backstepping control of a McKibben actuator driving an inertial load. In *ASME 2002 International Mechanical Engineering Congress and Exposition*, pages 381–386. American Society of Mechanical Engineers Digital Collection, 2002.

[63] D. Reynolds, D. Repperger, C. Phillips, and G. Bandry. Modeling the dynamic characteristics of pneumatic muscle. *Annals of biomedical engineering*, 31(3):310–317, 2003.

[64] R. M. Robinson, C. S. Kothera, R. M. Sanner, and N. M. Wereley. Nonlinear control of robotic manipulators driven by pneumatic artificial muscles. *IEEE/ASME Transactions on Mechatronics*, 21(1):55–68, 2015.

[65] D. Ryu, K.-W. Moon, H. Nam, Y. Lee, C. Chun, S. Kang, and J.-B. Song. Micro hydraulic system using slim artificial muscles for a wearable haptic glove. In *2008 IEEE/RSJ International Conference on Intelligent Robots and Systems*, pages 3028–3033. IEEE, 2008.

[66] N. Saga, T. Saikawa, and H. Okano. Flexor mechanism of robot arm using pneumatic muscle actuators. In *IEEE International Conference Mechatronics and Automation, 2005*, volume 3, pages 1261–1266. IEEE, 2005.

[67] J. Sárosi, I. Biro, J. Nemeth, and L. Cveticanin. Dynamic modeling of a pneumatic muscle actuator with two-direction motion. *Mechanism and Machine Theory*, 85:25–34, 2015.

[68] P. Scarfe and E. Lindsay. Air muscle actuated low cost humanoid hand. *International Journal of Advanced Robotic Systems*, 3(2):22, 2006.

[69] D. Schindele and H. Aschemann. Nonlinear model predictive control of a high-speed linear axis driven by pneumatic muscles. In *2008 American Control Conference*, pages 3017–3022. IEEE, 2008.

[70] H. Schulte. The characteristics of the McKibben artificial muscle, in: The application of External Power in Prosthetics and Orthotics. *National Academy of Sciences-National Research Council, Washington DC, Appendix H*, pages 94–115, 1961.

[71] Shadow. Shadow robotic company, 2020.

[72] Z. Situm and S. Herceg. Design and control of a manipulator arm driven by pneumatic muscle actuators. In *2008 16th Mediterranean Conference on Control and Automation*, pages 926–931. IEEE, 2008.

[73] J. E. Slightam, M. L. Nagurka, and E. J. Barth. Sliding mode impedance control of a hydraulic artificial muscle. In *ASME 2018 Dynamic Systems and Control Conference*. American Society of Mechanical Engineers Digital Collection, 2018.

[74] S. Sridar, C. J. Majeika, P. Schaffer, M. Bowers, S. Ueda, A. J. Barth, J. L. Sorrells, J. T. Wu, T. R. Hunt, and M. Popovic. Hydro Muscle-a novel soft fluidic actuator. In *2016 IEEE International Conference on Robotics and Automation (ICRA)*, pages 4014–4021. IEEE, 2016.

[75] T. D. C. Thanh and K. K. Ahn. Nonlinear PID control to improve the control performance of 2 axes pneumatic artificial muscle manipulator using neural network. *Mechatronics*, 16(9):577–587, 2006.

[76] R. Tiwari, M. A. Meller, K. B. Wajcs, C. Moses, I. Reveles, and E. Garcia. Hydraulic artificial muscles. *Journal of Intelligent Material Systems and Structures*, 23(3):301–312, 2012.

[77] B. Tondu and P. Lopez. The mckibben muscle and its use in actuating robot-arms showing similarities with human arm behaviour. *Industrial Robot: An International Journal*, 1997.

[78] B. Tondu and P. Lopez. Modeling and control of mckibben artificial muscle robot actuators. *IEEE control systems Magazine*, 20(2):15–38, 2000.

[79] G. Tonietti and A. Bicchi. Adaptive simultaneous position and stiffness control for a soft robot arm. In *IEEE/RSJ International Conference on Intelligent Robots and Systems*, volume 2, pages 1992–1997. IEEE, 2002.

[80] D. Trivedi, A. Lotfi, and C. D. Rahn. Geometrically exact dynamic models for soft robotic manipulators. In *2007 IEEE/RSJ International Conference on Intelligent Robots and Systems*, pages 1497–1502. IEEE, 2007.

[81] N. G. Tsagarakis and D. G. Caldwell. Development and control of a 'soft-actuated'exoskeleton for use in physiotherapy and training. *Autonomous Robots*, 15(1):21–33, 2003.

[82] N. S. Usevitch, A. M. Okamura, and E. W. Hawkes. APAM: antagonistic pneumatic artificial muscle. In *2018 IEEE International Conference on Robotics and Automation (ICRA)*, pages 1539–1546. IEEE, 2018.

[83] B. Verrelst, R. Van Ham, B. Vanderborght, F. Daerden, D. Lefeber, and J. Vermeulen. The pneumatic biped "Lucy" actuated with pleated pneumatic artificial muscles. *Autonomous Robots*, 18(2):201–213, 2005.

[84] B. Wang, W. Zhou, Y. Jin, H. Xu, and H. Ke. Modeling and characteristics analysis of intelligent pneumatic muscle with shape memory alloy braided shell. In *2009 International Asia Conference on Informatics in Control, Automation and Robotics*, pages 3–7. IEEE, 2009.

[85] C. Xiang, M. E. Giannaccini, T. Theodoridis, L. Hao, S. Nefti-Meziani, and S. Davis. Variable stiffness McKibben muscles with hydraulic and pneumatic operating modes. *Advanced Robotics*, 30(13):889–899, 2016.

[86] S. Xie, J. Mei, H. Liu, and Y. Wang. Hysteresis modeling and trajectory tracking control of the pneumatic muscle actuator using modified Prandtl–Ishlinskii model. *Mechanism and Machine Theory*, 120:213–224, 2018.

[87] L. A. Zadeh. Fuzzy sets. *Information and control*, 8(3):338–353, 1965.

[88] L. A. Zadeh. Fuzzy logic. *Computer*, 21(4):83–93, 1988.

[89] J. Zhang and Q. Zhang. Simulation of a muscle joint directly or indirectly driven by pneumatic pressure. *Acta mechanica*, 197(1-2):119–130, 2008.

[90] J.-F. Zhang, C.-J. Yang, Y. Chen, Y. Zhang, and Y.-M. Dong. Modeling and control of a curved pneumatic muscle actuator for wearable elbow exoskeleton. *Mechatronics*, 18(8):448–457, 2008.

[91] Z. Zhang and M. Philen. Pressurized artificial muscles. *Journal of Intelligent Material Systems and Structures*, 23(3):255–268, 2012.